

40p
N63-14872
code-1

NATIONAL AERONAUTICS AND SPACE ADMINISTRATION

TECHNICAL REPORT
R-101

THEORETICAL PREDICTION OF THE EFFECTS OF VORTEX FLOWS ON THE LOADING, FORCES, AND MOMENTS OF SLENDER AIRCRAFT

By J. RICHARD SPAHR

1961

Code 1

SINGLE COPY ONLY

TECHNICAL REPORT R-101

THEORETICAL PREDICTION OF THE EFFECTS OF VORTEX FLOWS ON THE LOADING, FORCES, AND MOMENTS OF SLENDER AIRCRAFT

By J. RICHARD SPAHR

**Ames Research Center
Moffett Field, Calif.**

CONTENTS

	Page
SUMMARY.....	1
INTRODUCTION.....	1
NOTATION.....	2
Subscripts.....	3
THEORETICAL CONSIDERATIONS.....	4
Slender-Body Method.....	4
Initial vortex strengths and positions.....	4
Vortex paths.....	5
Load distributions due to vortices.....	6
Forces and moments due to vortices.....	8
Linear-Theory Method.....	8
APPLICATION AND EVALUATION OF SLENDER-BODY METHOD.....	9
Scope and Procedure.....	9
Vortex Paths.....	14
Vortices of various strengths.....	14
Vortices of various initial positions.....	15
Angles of roll.....	15
Angles of pitch.....	16
Wings of various aspect ratios.....	18
Comparisons of calculated and measured vortex paths.....	18
Load Distributions, Forces, and Moments Due to Vortices.....	20
Vortices of various strengths.....	20
Vortices of various initial positions.....	21
Angles of roll.....	21
Angles of pitch.....	22
Wings of various aspect ratios.....	23
Comparisons of calculated results with experiment.....	29
CONCLUDING REMARKS.....	31
REFERENCES.....	35
TABLE I.—EXPRESSIONS FOR POTENTIAL-FLOW VELOCITY COMPONENTS ON SURFACES OF WING-BODY COMBINATIONS..	36
TABLE II.—VORTEX STRENGTHS AND INITIAL POSITIONS ($x=0$)....	37

TECHNICAL REPORT R-101

THEORETICAL PREDICTION OF THE EFFECTS OF VORTEX FLOWS ON THE LOADING, FORCES, AND MOMENTS OF SLENDER AIRCRAFT

BY J. RICHARD SPAHR

SUMMARY

14872

A general calculative method based on slender-body theory is developed for predicting the paths of vortices in the presence of wing-body combinations at subsonic, transonic, and supersonic speeds and the influence of the vortices on the loading, forces, and moments acting on the combinations. The method is applied to wing-body combinations to study the effects of vortex strength and initial position, combined angles of pitch and roll, and wing aspect ratio on the vortex paths and induced loads. The results indicate that these effects were significant because of the dependence of the vortex paths and induced loads on the vortex strengths and on the proximity of the vortices to the surface of a wing-body combination.

Comparisons of theoretical and experimental results indicated that the vortex paths and vortex-induced forces and moments for slender-wing-body combinations were closely predicted by the slender-body method, but for nonslender combinations these characteristics were only approximated. The application of an alternate method based on reverse-flow theory improved the predictions of the vortex-induced forces and moments for the latter combinations but impaired those for slender combinations. The induced forces and moments on the nonslender combinations were sufficiently small that the total forces and moments could be predicted adequately through the use of either method.

INTRODUCTION

The effects of vortex-interference flows generally must be calculated in order to predict successfully the aerodynamic loading, forces, and stability characteristics of airplanes or missiles. For example, the results of references 1 and 2 showed that

it was necessary to include estimates of the effects of the vortices generated by the forebody or forward lifting surfaces in the prediction of the lift and pitching moments of various wing-body or wing-body-tail combinations.

Two fundamentally different theoretical methods, each involving some basic limitations, exist for calculating the vortex-induced forces and moments on wing-body-tail combinations. One method, which is based on linearized wing theory, makes use of a reverse-flow theorem (refs. 3 and 4), for calculating the forces and two-dimensional strip theory for calculating the moments. It is assumed that the vortex paths are known and that these paths are parallel to a chord of the wing panels near which the vortices pass. Additional assumptions are involved in estimating the influence of the body. This method has been used successfully in the prediction of the aerodynamic characteristics of combinations having wing or tail surfaces of high or moderate aspect ratio, in which cases the deviations of the actual vortex paths from the assumed paths were relatively unimportant. The other theoretical method for calculating the vortex-induced forces and moments on wing-body or wing-body-tail combinations is based on slender-body theory (ref. 5). This method represents a more complete solution to the vortex-interference problem for slender configurations primarily because it takes into account the actual predetermined vortex paths which may be influenced significantly by the local flow field of the combination. No theoretical method has heretofore been developed for calculating the load distributions on wing-body combinations due to vortices.

The present investigation was undertaken to achieve the following objectives: (1) development of a general method based on slender-body theory for calculating the paths of vortices in the presence of wing-body combinations and for computing the effects of these vortices on the load distributions, forces, and stability of complete configurations; (2) application of this method to the calculation of vortex paths and induced loads on various wing-body combinations; and (3) evaluation of the method by comparisons of vortex paths, forces, and moments calculated by this method with those calculated by alternate theoretical methods and with available experimental results for several representative configurations.

NOTATION

a	body radius	C_Y	side-force coefficient, $\frac{\text{force in the } y \text{ direction}}{qS}$ (See fig. 1.)
A	wing aspect ratio	C_Γ	vortex-strength coefficient, $\frac{\Gamma}{2\pi Va}$
B	$\sqrt{M^2 - 1}$	d	body diameter
c	local wing chord	i_v	vortex interference factor
c_n	section normal-force coefficient, $\frac{\text{force per unit span in } z \text{ direction}}{qc}$	$\Pi ()$	imaginary part
c_r	chord at wing-body juncture	k_w	ratio of lift of wing in presence of body to lift of wing alone for variable wing incidence
C_L	rolling-moment coefficient, $\frac{\text{moment about } x \text{ axis}}{qSd}$ (See fig. 1.)	K_w	ratio of lift of wing in presence of body to lift of wing alone for variable angle of attack
C_m	pitching-moment coefficient, $\frac{\text{moment about } y \text{ axis}}{qSd}$ (See fig. 1.)	K_ϕ	lift ratio accounting for the additional lift due to sideslip at a constant angle of attack
C_N	normal-force coefficient, $\frac{\text{force in the } z \text{ direction}}{qS}$ (See fig. 1.)	L.E.	leading edge
C_{N_α}	normal-force curve slope, $\frac{dC_N}{d\alpha}$	M	free-stream Mach number
C_n	yawing-moment coefficient, $\frac{\text{moment about } z \text{ axis}}{qSd}$ (See fig. 1.)	p	local surface static pressure
C_p	pressure coefficient, $\frac{p-p_0}{q}$	p_0	free-stream static pressure
		q	free-stream dynamic pressure
		r	radius of body in transformed-circle plane
		r_v	initial radial position of vortex
		s	local wing semispan (See fig. 1.)
		S	body cross-sectional area
		$u, v, w,$	perturbation velocity components in the x, y, z directions, respectively
		V	free-stream velocity
		x, y, z	Cartesian coordinates fixed in the body (See fig. 1.)
		x_n	axial distance from body apex
		x_s	axial distance from body apex to vortex flow separation point
		α	angle of attack (See fig. 1.)
		β	angle of sideslip (See fig. 1.)
		Γ	vortex strength
		δ	canard incidence
		ϵ	wing semiapex angle
		ζ	complex coordinate, $y + iz$
		θ	angle of pitch, $(\alpha^2 + \beta^2)^{1/2}$
		ρ	initial angular position of vortex
		σ	complex coordinate in transformed circle plane (See sketch (a).)

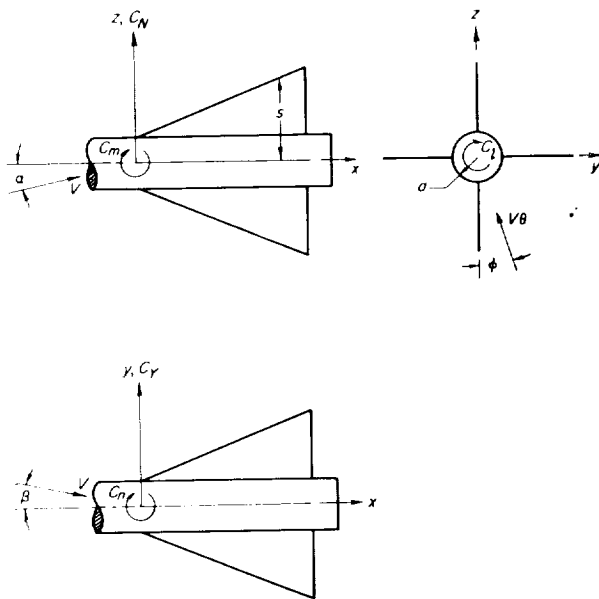
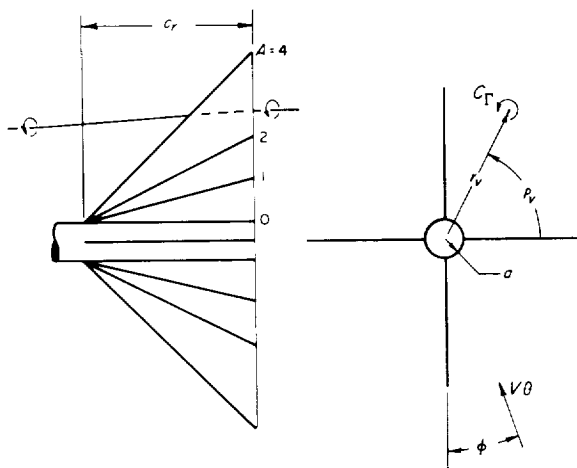


FIGURE 1.—Coordinate system.

Values of Parameters Investigated		
Parameter	Basic Value	Range in Value
Wing root chord, $C_{r/a}$	—	0 to 10
Angle of roll, ϕ		
Cruciform wing	0 and 15°	0 to 45°
Planar wing	0	0 to 90°
Angle of pitch, θ	20°	10° to 30°
Wing aspect ratio, A	2	0 to 4
Vortex strength, C_r	± 0.263	0 to ± 0.395
Initial vortex position		
Radial position, r/a	1.61	—
Angular position, ρ_v	$(\phi + 90^\circ) \pm 25^\circ$	$(\phi + 90^\circ) \pm (20^\circ \text{ to } 30^\circ)$



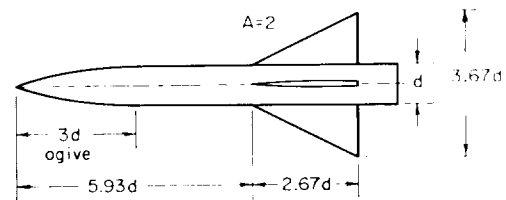
(a) Configuration A.

FIGURE 2.—Configurations studied.

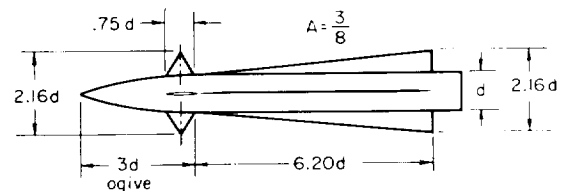
ϕ angle of roll (See fig. 2(a).)
 ψ, ω velocity components in the σ plane corresponding to v, w in the ξ plane
 $(\bar{\cdot})$ conjugate of a complex variable (e.g., $\bar{\xi} = y - iz$)

SUBSCRIPTS

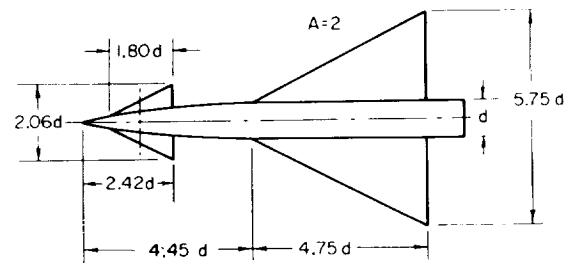
B body
 BC body-canard combination
 BW body-wing combination
 BWC body-wing-canard combination
 L lower surface
 U upper surface
 v vortex
 W wing alone
 $W(B)$ wing in presence of body
 α angle of attack
 β angle of sideslip
 1 vortex 1 (See sketch (b).)
 2 vortex 2 (See sketch (b).)



(b) Configuration B.



(c) Configuration C.



(d) Configuration D.

FIGURE 2.—Concluded.

THEORETICAL CONSIDERATIONS

A theoretical method is described for calculating the paths of vortices and the influence of the vortices on the loading, forces, and moments acting on wing-body combinations. The method is developed within the framework of slender-body theory and is thus applicable to smooth slender configurations of arbitrary cross section. The general calculative procedure consists of the following steps:

- (1) Determination of the initial positions and strengths of the vortices generated by the forebody or canard surfaces
- (2) Calculation of the vortex paths in the presence of the wing-body combination
- (3) Calculation of the spanwise load distribution or the forces and moments induced by the vortices.

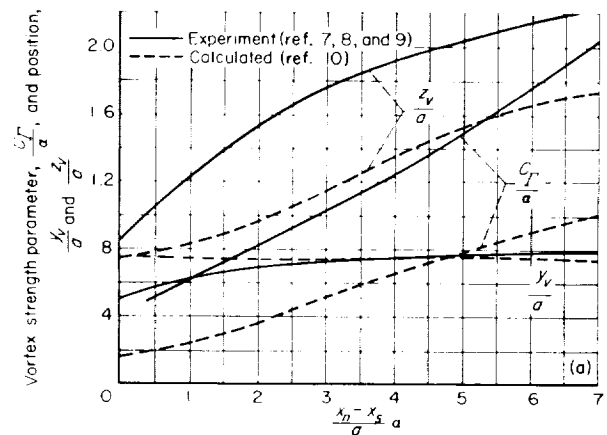
A description of the method along with an alternate method for estimating the vortex-induced forces and moments is presented in the following paragraphs.

SLENDER-BODY METHOD

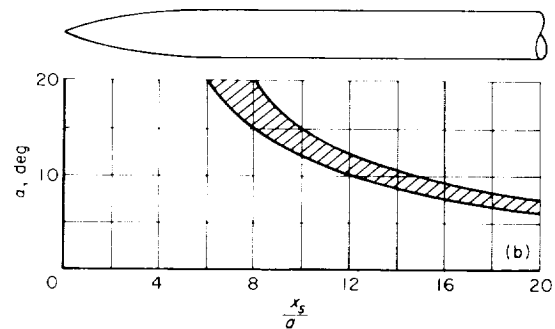
Initial vortex strengths and positions.—To calculate the path of a vortex in the vicinity of a wing-body combination, it is first necessary to know the strength and position of the vortex in the plane for which the calculations are to be started. In the present study, this plane is assumed to be normal to the body axis at the leading edge of the wing-body juncture. One or more pairs of vortices may be generated by a forebody or by a body-canard combination ahead of the wing.

In the case of a forebody at moderate angles of attack, a pair of vortices due to boundary-layer separation is formed along the lee side of the body, and these vortices move away from the body as they progress downstream. A corresponding increase in the vortex strength occurs as a result of the feeding action of the small vortex filaments interconnecting the body boundary layer and the vortex cores. Although no completely theoretical method exists for calculating the strength and position of body vortices, the analysis reported in reference 6 has shown that the vortex coordinates y_v/a and z_v/a and the vortex strength parameter C_T/α for a body of circular cross section are functions only of the dimensionless parameter $\alpha(x_n - x_s)/a$. It has been found that the experimental

results given in references 7, 8, and 9 for various angles of attack and forebody shapes correlate successfully by means of this parameter. The resulting correlation curves are presented in figure 3(a).



(a) Vortex strength and position for ogive-cylinders and cone-cylinders.



(b) Axial location of vortex separation for ogive-cylinder of reference 6; $M = 2$.

FIGURE 3.—Vortex characteristics of bodies of revolution.

The location of the vortex-separation point x_s was found in reference 7 to move forward with increasing angle of attack and to lie within the region shown in figure 3(b). It was also shown in reference 7 that the observed vortex paths could be predicted satisfactorily by means of a stepwise numerical method based on two-dimensional incompressible-flow theory. This method, however, requires the use of experimental values for the vortex-separation point x_s (fig. 3(b)) and for the body cross-flow drag coefficients. In reference 10, a theoretical method is developed for calculating both the strength and positions of vortices from circular cylinders and cones for which only the peripheral location on the body of the vortex sepa-

ration point must be determined from experiment. Some results computed by this method are shown in figure 3(a) for comparison with experiment. Comparison indicates that the strength and vertical displacement of the body vortices are considerably underestimated by the method of reference 10.

The results given in figure 3 may also be used for bodies of revolution at combined angles of attack and sideslip provided the angle of pitch θ is substituted for the angle of attack α and the vortex positions y_v and z_v are rotated through the angle φ at a constant radial location. The approximate relationships among these angles are

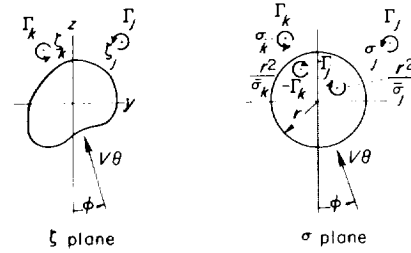
$$\theta = \sqrt{\alpha^2 + \beta^2} \quad (1)$$

$$\varphi = \tan^{-1} \frac{\beta}{\alpha} \quad (2)$$

For body-canard combinations the induced vortex flow field can generally be represented by a single line vortex originating from the trailing edge of each canard panel, because in most cases the body cross-flow vortices are relatively weak and the trailing vortex sheet from the canard panel is essentially rolled up into a single vortex at the wing location. The strengths and initial spanwise locations of these vortices are calculated directly from the lift and spanwise circulation distribution of the canard surfaces in the presence of the body. A theoretical method is presented in reference 2 for calculating the strengths and positions of the vortices trailing from a canard-body combination at zero sideslip as functions of the lift and spanwise load distribution of the canard surfaces due to angle of attack and incidence. This method is applicable to configurations in sideslip as well as those at zero sideslip since the theoretical spanwise circulation distribution is the same as the spanwise load distribution for zero sideslip and is independent of sideslip.

Vortex paths.—The determination of the paths of vortices in the presence of a body or wing-body combination requires a stepwise numerical calculation of the vortex positions at successive streamwise locations. For slender configurations, a method is developed for computing these paths on the basis of the analysis of reference 11 which treats the motion of vortices in the presence of solid boundaries in two-dimensional incompressible flow.

Consider first the flow in a crossflow plane of a body of arbitrary cross section in the presence of m vortices of known strengths Γ_j , Γ_k and positions ζ_j , ζ_k as shown in sketch (a) for both the physical and transformed circle planes. Image vortices are required inside the circle in the σ plane to satisfy the boundary condition of no flow through the body surface. The product $V\theta$ represents the component of the free-stream velocity in the crossflow plane.



Sketch (a)

The calculation of the change in position of a vortex (e.g., vortex j) in the ζ plane as it progresses an incremental distance Δx downstream is given by the expression

$$\Delta \zeta_j = \left(\frac{v_j}{V} + i \frac{w_j}{V} \right) \Delta x \quad (3)$$

where v_j and w_j are the components of the resultant velocity at the vortex position ζ_j . It is shown in reference 11 that these velocity components in the ζ plane can be obtained from those in the σ plane by the relationship

$$v_j - iw_j = (\psi_j - i\omega_j) \left(\frac{d\sigma}{d\zeta} \right)_j - \frac{i\Gamma_j}{4\pi} \left(\frac{d^2\sigma}{d\zeta^2} \right)_j \quad (4)$$

where

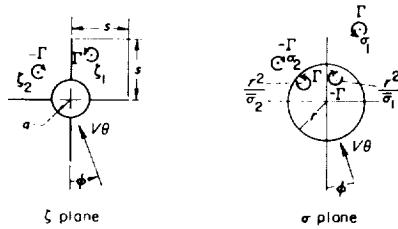
$$\psi_j - i\omega_j = -iV\theta \left(e^{-i\varphi} + \frac{r^2}{\sigma_j^2} e^{i\varphi} \right) - \frac{i}{2\pi} \left(\sum_{k=1}^m \frac{\Gamma_k}{\sigma_j - \sigma_k} - \sum_{k=1}^m \frac{\Gamma_k}{\sigma_j - \frac{r^2}{\sigma_k}} \right) \quad (5)$$

The first two terms in equation (5) give the velocity at the vortex location σ_j due to the crossflow component of the free-stream velocity $V\theta$, and the remaining terms account for the velocity at σ_j due

to all of the other vortices in the system. The last term in equation (4) represents the reaction from the body upon vortex j due to the effect of this vortex.

The general expressions given by equations (3) to (5) can be applied to the stepwise numerical calculation of the paths of vortices of known strength and initial position in the presence of a body or wing-body combination for which the conformal transformation of the cross section to a circle is known. General expressions are given in references 12 to 15 for such transformations for a wide variety of body and wing-body combinations. For the special case of a circular body, equations (4) and (5) simplify to those used in references 7 and 16 to calculate the paths of vortices in the presence of a body of revolution.

As an illustration of the application of the general expressions for calculating vortex paths, consider two vortices having strengths of equal magnitude but of opposite sense in the presence of a circular-body and cruciform-wing combination inclined in both pitch and roll with respect to the free stream, as shown in sketch (b). The change



Sketch (b)

in position of vortex 1 in the distance Δx is given by equation (3) as

$$\Delta \zeta_1 = \left(\frac{v_1}{V} + i \frac{w_1}{V} \right) \Delta x \quad (6)$$

where the velocities in the ζ and σ planes, respectively, are given by equations (4) and (5) as

$$v_1 - iw_1 = (\psi_1 - i\omega_1) \left(\frac{d\sigma}{d\zeta} \right)_1 - \frac{i\Gamma}{4\pi} \frac{\left(\frac{d^2\sigma}{d\zeta^2} \right)_1}{\left(\frac{d\sigma}{d\zeta} \right)_1} \quad (7)$$

and

$$\psi_1 - i\omega_1 = -iV\theta \left(e^{-i\varphi} + \frac{r^2}{\sigma_1^2} e^{i\varphi} \right) - \frac{i\Gamma}{2\pi} \left(-\frac{1}{\sigma_1 - \frac{r^2}{\sigma_1}} - \frac{1}{\sigma_1 - \sigma_2} + \frac{1}{\sigma_1 - \frac{r^2}{\sigma_2}} \right) \quad (8)$$

The conformal mapping function relating the ζ and σ planes is (ref. 12)

$$\zeta^2 \left(1 + \frac{a^4}{\zeta^4} \right) = \sigma^2 \left(1 + \frac{r^4}{\sigma^4} \right) \quad (9)$$

where

$$r^2 = \frac{1}{2} s^2 \left(1 + \frac{a^4}{s^4} \right) \quad (10)$$

Differentiation of equation (9) once gives

$$\frac{d\sigma}{d\zeta} = \frac{\zeta}{\sigma} \frac{1 - \frac{a^4}{\zeta^4}}{1 - \frac{r^4}{\sigma^4}} \quad (11)$$

and a second time gives

$$\frac{d^2\sigma}{d\zeta^2} = \frac{d\sigma}{d\zeta} \left[\frac{1}{\sigma} \left(3 - \frac{4}{1 - \frac{r^4}{\sigma^4}} \right) \frac{d\sigma}{d\zeta} - \frac{1}{\zeta} \left(3 - \frac{4}{1 - \frac{a^4}{\zeta^4}} \right) \right] \quad (12)$$

The corresponding conformal-mapping relationships for a planar wing-body combination (no vertical wing panels) are

$$\zeta + \frac{a^2}{\zeta} = \sigma + \frac{r^2}{\sigma} \quad (13)$$

where

$$r = \frac{1}{2} s \left(1 + \frac{a^2}{s^2} \right) \quad (14)$$

$$\frac{d\sigma}{d\zeta} = \frac{1 - \frac{a^2}{\zeta^2}}{1 - \frac{r^2}{\sigma^2}} \quad (15)$$

$$\frac{d^2\sigma}{d\zeta^2} = 2 \frac{d\sigma}{d\zeta} \left[\frac{1}{\sigma \left(1 - \frac{\sigma^2}{r^2} \right)} \frac{d\sigma}{d\zeta} - \frac{1}{\zeta \left(1 - \frac{\zeta^2}{a^2} \right)} \right] \quad (16)$$

Load distributions due to vortices.—Once the positions of the vortices ζ_k in a given crossflow

plane have been determined for a slender wing-body combination the pressure and hence the loading at any point along the body and wing panel in this plane can be calculated by slender-body theory.

The pressure coefficient at any point on an arbitrary body inclined at an angle of attack α and sideslip β is given by the general expression

$$C_p = -\frac{2}{V^2} (u + \alpha w - \beta v) - \frac{1}{V^2} (v^2 + w^2) \quad (17)$$

where the perturbation velocities u, v, w represent the local velocities and those at infinity. Each of the velocity components can be considered to be made up of three parts, one due to angle of attack, one due to angle of sideslip, and one due to the vortices. Thus,

$$\left. \begin{aligned} u &= u_\alpha + u_\beta + u_v \\ v &= v_\alpha + v_\beta + v_v \\ w &= w_\alpha + w_\beta + w_v \end{aligned} \right\} \quad (18)$$

The loading coefficient at a given spanwise location is then computed from

$$\frac{\Delta p}{q} = C_{pL} - C_{pU} \quad (19)$$

For bodies or body-wing combinations symmetrical about both the vertical and horizontal planes, the following conditions are applicable:

$$\left. \begin{aligned} u_{\alpha L} &= -u_{\alpha U} & u_{\beta L} &= u_{\beta U} \\ v_{\alpha L} &= -v_{\alpha U} & v_{\beta L} &= v_{\beta U} \\ w_{\alpha L} &= w_{\alpha U} & w_{\beta L} &= -w_{\beta U} \end{aligned} \right\} \quad (20)$$

Substitution of equations (17), (18), and (20) into equation (19) gives for the total loading

$$\begin{aligned} \frac{\Delta p}{q} &= \frac{4}{V^2} (u_{\alpha U} + \alpha w_{\beta U} - \beta v_{\alpha U}) + \frac{4}{V^2} (v_{\alpha U} v_{\beta U} + w_{\alpha U} w_{\beta U}) \\ &+ \frac{2}{V^2} (u_{rU} - u_{rL}) + \frac{1}{V^2} [(v_{rU}^2 + w_{rU}^2) - (v_{rL}^2 + w_{rL}^2)] \\ &+ 2v_{\alpha U} (v_{rU} + v_{rL}) + 2w_{\beta U} (w_{rU} + w_{rL}) \\ &+ 2(v_{\beta U} - V\beta) (v_{rU} - v_{rL}) + 2(w_{\alpha U} + V\alpha) (w_{rU} - w_{rL}) \end{aligned} \quad (21)$$

The first two terms in this equation represent the loading due to the flow in the absence of vortices

and the remaining terms account for the additional loading due to the vortices. On the surface of a horizontal wing panel ($z=0$), equation (21) simplifies to

$$\begin{aligned} \frac{\Delta p}{q} &= \frac{4}{V^2} (u_{\alpha U} - \beta v_{\alpha U}) + \frac{4}{V^2} v_{\alpha U} v_{\beta U} + \frac{2}{V^2} (u_{rU} - u_{rL}) \\ &+ \frac{1}{V^2} [v_{rU}^2 - v_{rL}^2 + 2v_{\alpha U} (v_{rU} + v_{rL}) \\ &+ 2(v_{\beta U} - V\beta) (v_{rU} - v_{rL})] \end{aligned} \quad (22)$$

and on the surface of a body of revolution of radius a the loading at a given value of y is

$$\begin{aligned} \frac{\Delta p}{q} &= \frac{4}{V^2} u_{\alpha U} + \frac{4}{V^2} \frac{a^2}{a^2 - y^2} v_{\alpha U} (v_{\beta U} - V\beta) + \frac{2}{V^2} (u_{rU} - u_{rL}) \\ &+ \frac{1}{V^2} \frac{a^2}{a^2 - y^2} [v_{rU}^2 - v_{rL}^2 + 2v_{\alpha U} (v_{rU} + v_{rL}) \\ &+ 2(v_{\beta U} - V\beta) (v_{rU} - v_{rL})] \end{aligned} \quad (23)$$

General expressions for the velocity components for calculation of the loading from equation (20), (21), or (22) are

$$u_\alpha = \frac{V\alpha}{2\pi(\sigma)} \frac{dr^2}{dx} \quad (24)$$

$$(w_\alpha + V\alpha) + iv_\alpha = V\alpha \left(1 + \frac{r^2}{\sigma^2} \right) \frac{d\sigma}{d\zeta} \quad (25)$$

$$(v_\beta - V\beta) - iw_\beta = -V\beta \left(1 - \frac{r^2}{\sigma^2} \right) \frac{d\sigma}{d\zeta} \quad (26)$$

$$\begin{aligned} u_{rU} &= \frac{1}{2\pi} \Pi \sum_{k=1}^m \Gamma_k \left[\frac{1}{\sigma - \sigma_k} \left(\frac{d\sigma}{dx} - \frac{d\sigma_k}{dx} \right) \right. \\ &\quad \left. - \frac{1}{r^2} \left(\frac{d\sigma}{dx} + \frac{r^2}{\sigma_k^2} \frac{d\sigma_k}{dx} - \frac{1}{\sigma_k} \frac{dr^2}{dx} \right) \right] \end{aligned} \quad (27)$$

$$\begin{aligned} u_{rL} &= \frac{1}{2\pi} \Pi \sum_{k=1}^m \Gamma_k \left[\frac{1}{\sigma - \sigma_k} \left(\frac{d\sigma}{dx} - \frac{d\sigma_k}{dx} \right) \right. \\ &\quad \left. - \frac{1}{r^2} \left(\frac{d\sigma}{dx} + \frac{r^2}{\sigma_k^2} \frac{d\sigma_k}{dx} - \frac{1}{\sigma_k} \frac{dr^2}{dx} \right) \right] \end{aligned} \quad (28)$$

$$w_{rU} + iv_{rU} = \frac{1}{2\pi} \sum_{k=1}^m \Gamma_k \left(\frac{1}{\sigma - \sigma_k} - \frac{1}{\sigma - \frac{r^2}{\sigma_k}} \right) \frac{d\sigma}{d\zeta} \quad (29)$$

$$w_{rL} + iv_{rL} = \frac{1}{2\pi} \sum_{k=1}^m \Gamma_k \left(\frac{1}{\sigma - \sigma_k} - \frac{1}{\sigma - \frac{r^2}{\sigma_k}} \right) \left(\frac{d\sigma}{d\zeta} \right) \quad (30)$$

Evaluation of these velocities requires only a knowledge of the conformal transformation between the configuration cross section and a circle. For a cruciform or planar wing in combination with a body of circular cross section, expressions were given in equations (9), (10), (13), and (14) for the transformations. These equations can be combined with equations (24), (25), and (26) to give expressions for the potential-flow velocity components in terms of the physical-plane coordinates. The resulting expressions are presented in table I.

Forces and moments due to vortices.—The forces and moments acting on the wing or body of a combination due to vortices are obtained from integrations of the load distributions computed from the foregoing relations. However, the forces and moments due to vortices acting on the complete combination can be obtained directly from the vortex positions with the use of the slender-body analysis of reference 5. It is shown in this analysis that the side force and normal force due to m vortices acting on a slender body are given by

$$C_Y + iC_N = \frac{2i}{V} \left\{ \left[\sum_{k=1}^m \Gamma_k \left(\sigma_k - \frac{r^2}{\sigma_k} \right) \right]_{x=c_r} - \left[\sum_{k=1}^m \Gamma_k \left(\sigma_k - \frac{r^2}{\sigma_k} \right) \right]_{x=0} \right\} \quad (31)$$

and the corresponding moments are given by

$$C_n + iC_m = \frac{2i}{Vd} \int_0^{c_r} x dx \left[\sum_{k=1}^m \Gamma_k \left(\sigma_k - \frac{r^2}{\sigma_k} \right) \right] dx \\ = -\frac{1}{d} \int_0^{c_r} x dx (C_Y + iC_N) \quad (32)$$

For the case of one pair of vortices these expressions reduce to

$$C_Y + iC_N = \frac{2i\Gamma}{V} \left[\left(\sigma_1 - \frac{r^2}{\sigma_1} - \sigma_2 + \frac{r^2}{\sigma_2} \right)_{x=c_r} - \left(\sigma_1 - \frac{r^2}{\sigma_1} - \sigma_2 + \frac{r^2}{\sigma_2} \right)_{x=0} \right] \quad (33)$$

and

$$C_n + iC_m = -\frac{2i\Gamma}{Vd} \int_0^{c_r} x dx \left(\sigma_1 - \frac{r^2}{\sigma_1} - \sigma_2 + \frac{r^2}{\sigma_2} \right) dx \quad (34)$$

It is noted from these equations that the forces due to the vortices along any portion of the con-

figuration can be calculated directly from the change in position of the vortices in the transformed circle plane between one x station and another. The calculation of the moments, however, requires an integration of these positions along the body. This integration can be performed simultaneously with the numerical stepwise calculation of the vortex paths by means of the relationship

$$(C_n + iC_m)_{n+1} = (C_n + iC_m)_n - \left(n + \frac{1}{2} \right) \frac{\Delta x}{d} [(C_Y + iC_N)_{n+1} - (C_Y + iC_N)_n] \quad (35)$$

where n is the number of streamwise intervals from the origin to the longitudinal station under consideration.

LINEAR-THEORY METHOD

The forces and moments acting on a wing-body combination in the presence of vortices are generally calculated by means of linearized wing theory for potential flow in conjunction with a reverse-flow theorem. (See, e.g., refs. 1 to 4.) In the application of this method, it is assumed that the paths of the vortices generated by the forward surfaces are not influenced by the trailing surfaces and that the flow angularity induced by the vortices varies only with the spanwise coordinate. In addition, the chordwise location of the vortex-induced load must be assumed in order to estimate the moments. These assumptions would be expected to be more valid for surfaces of high aspect ratio than those of low aspect ratio.

Consider a general wing-body combination as shown in figure 1. The normal force and pitching moment acting on the combination due to m vortices of given strength Γ_k and position (y_k, z_k) in the crossflow plane are given by

$$C_N = \frac{K_w}{S} \left[\int_a^s \frac{w}{V} \left(\frac{c_n c}{\alpha} \right)_w dy + \int_{-a}^{-s} \frac{w}{V} \left(\frac{c_n c}{\alpha} \right)_w dy \right] \quad (36)$$

and

$$C_m = -\frac{K_w}{Sd} \left[\int_a^s \frac{w}{V} \left(\frac{c_n c}{\alpha} \right)_w x_{cp} dy + \int_{-a}^{-s} \frac{w}{V} \left(\frac{c_n c}{\alpha} \right)_w x_{cp} dy \right] \quad (37)$$

The upwash w due to the vortices and their images is given by

$$w = \frac{1}{2\pi} \sum_{k=1}^m \Gamma_k \left[\frac{y-y_k}{(y-y_k)^2 + z_k^2} - \frac{y-y_i}{(y-y_i)^2 + z_i^2} \right] \quad (38)$$

where

$$y_i = -\frac{y_k a^2}{y_k^2 + z_k^2}; \quad z_i = \frac{z_k a^2}{y_k^2 + z_k^2} \quad (39)$$

The quantity $(c_n c / \alpha)_w$, which represents the span loading coefficient for the wing alone in reverse flow, is a function of the sideslip angle β . For many instances the shape of the span loading curve can be considered independent of sideslip with only the integrated load on each side of the combination being affected. In such cases

$$\frac{c_n c}{\alpha} = \frac{C_{N\alpha}}{C_{N\alpha, \beta=0}} \left(\frac{c_n c}{\alpha} \right)_{\beta=0} \quad (40)$$

and for slender wing panels, from reference 1,

$$\frac{C_{N\alpha}}{C_{N\alpha, \beta=0}} = 1 + \frac{K_\varphi}{\tan \epsilon} \beta \text{ on the right panel} \quad (41)$$

$$\frac{C_{N\alpha}}{C_{N\alpha, \beta=0}} = 1 - \frac{K_\varphi}{\tan \epsilon} \beta \text{ on the left panel} \quad (42)$$

where $K_\varphi = 2/\pi$ for a planar wing and 0.38 for a cruciform wing.

For many practical cases the span load distribution for the wing panels in reverse flow can be approximated by elementary analytical functions such as a straight line or ellipse. For such cases, equations (36) and (37) can be integrated in closed form. In reference 2, for example, solutions of equation (36) were obtained for various linear span load distributions, and charts were presented for the rapid determination of a vortex interference factor from which the normal force due to a symmetrical pair of vortices can be computed for wing-body combinations having bodies of circular cross section. Because of the vortex-symmetry requirement, application of these charts is limited to configurations at zero sideslip.

In order to extend the charts of reference 2 to the general case of combined angles of attack or canard deflections and sideslip angles, figures 4 and 5 have been prepared. These curves present values of the vortex interference factor i_v for the positive (right) half of the wing-body combination

under the influence of a single vortex at any position in the y - z plane. Values for the negative (left) half of the combination are obtained from these figures simply by a reversal in the sign of the lateral coordinate y . The curves of figures 4 and 5 are also applicable to negative values of z as well as positive values. Figure 4 presents interference factors for a triangular distribution of loading along the span (no load at wing tip), whereas figure 5 gives the corresponding results for a trapezoidal distribution for which the wing-tip load is one half that at the root. Auxiliary calculations of the interference factors for an elliptical load distribution have shown that the results were in such close agreement with those for a trapezoidal distribution that the curves of figure 5 can be applied to either type of distribution.

The curves of figures 4 and 5 can be employed to calculate the effect of any number of vortices of known strength and position on the normal-force coefficient of a wing-body combination by superposition. Thus, for m vortices

$$C_N = \frac{K_w}{2\pi V(s-a)} \left[\left(C_{N\alpha, w} \sum_{k=1}^m \Gamma_k i_{rk} \right)_R + \left(C_{N\alpha, w} \sum_{k=1}^m \Gamma_k i_{rk} \right)_L \right] \quad (43)$$

where the subscripts R and L refer to the right and left side, respectively, of the wing-body combination, and the interference factor i_v is defined as

$$i_v = \frac{2\pi(s-a)}{\Gamma C_{N\alpha, w} S} \int_a^s w \frac{c_n c}{\alpha} dy \quad (44)$$

Equation (43) in conjunction with figures 4 and 5 can also be used to determine the side-force coefficient C_Y due to an arbitrary system of vortices for the vertical surfaces of a wing-body or tail-body combination. In this case the quantity $C_{N\alpha, w}$ in equation (43) is replaced by $C_{Y\alpha, w}$ of the vertical surface, and the y and z coordinates of the vortices are interchanged when figures 4 and 5 are used to obtain values of i_v .

APPLICATION AND EVALUATION OF SLENDER-BODY METHOD

SCOPE AND PROCEDURE

The stepwise theoretical method based on slender-body theory has been applied to the

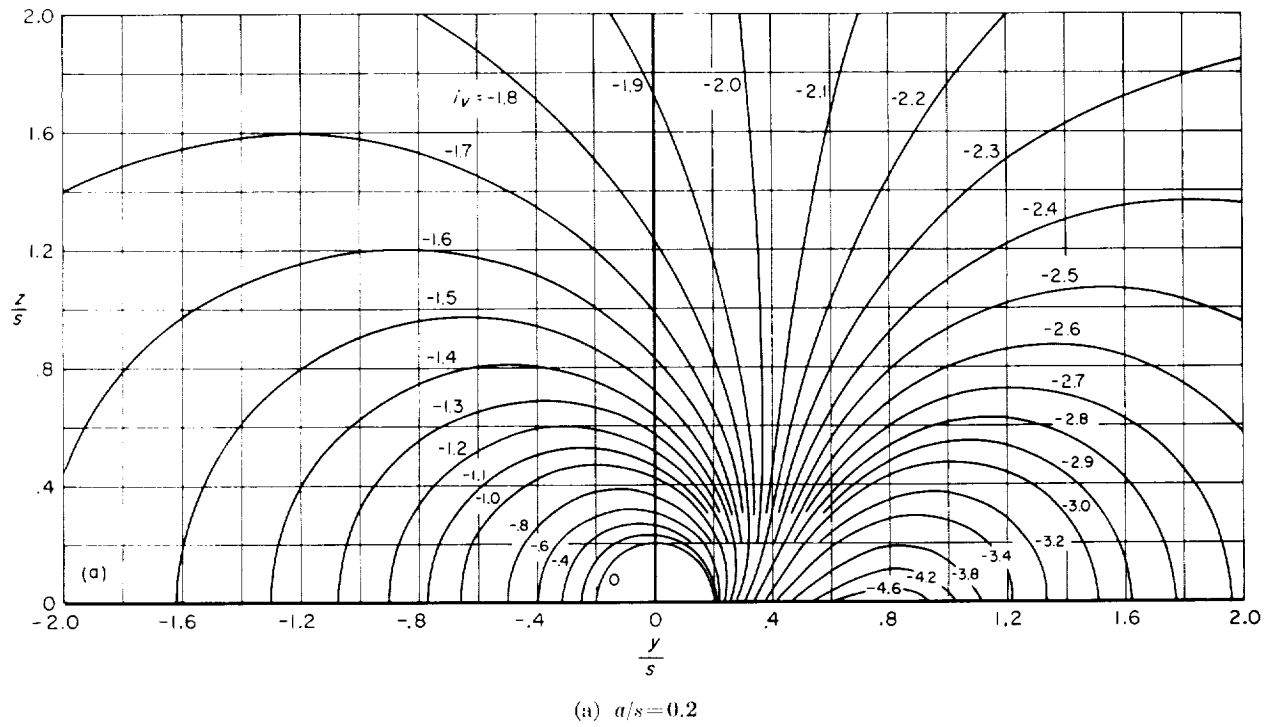


FIGURE 4. -Vortex-interference factors for triangular span load distribution.

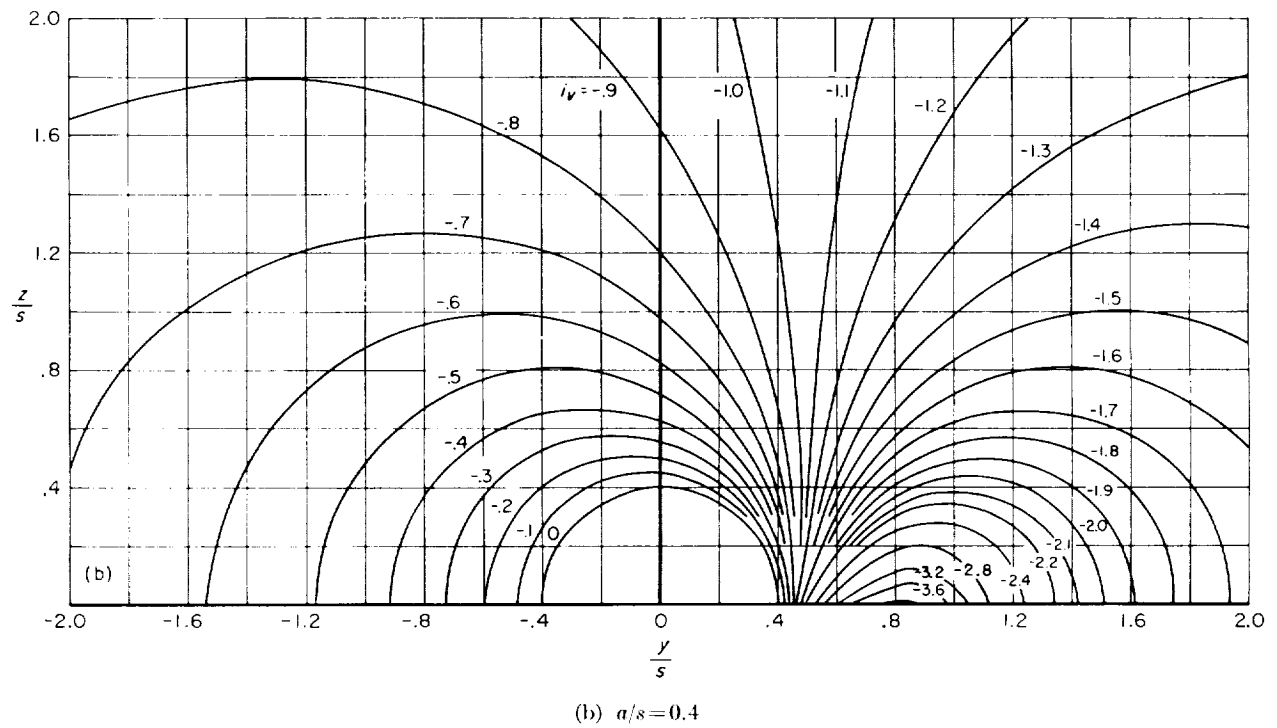


FIGURE 4. -Continued.

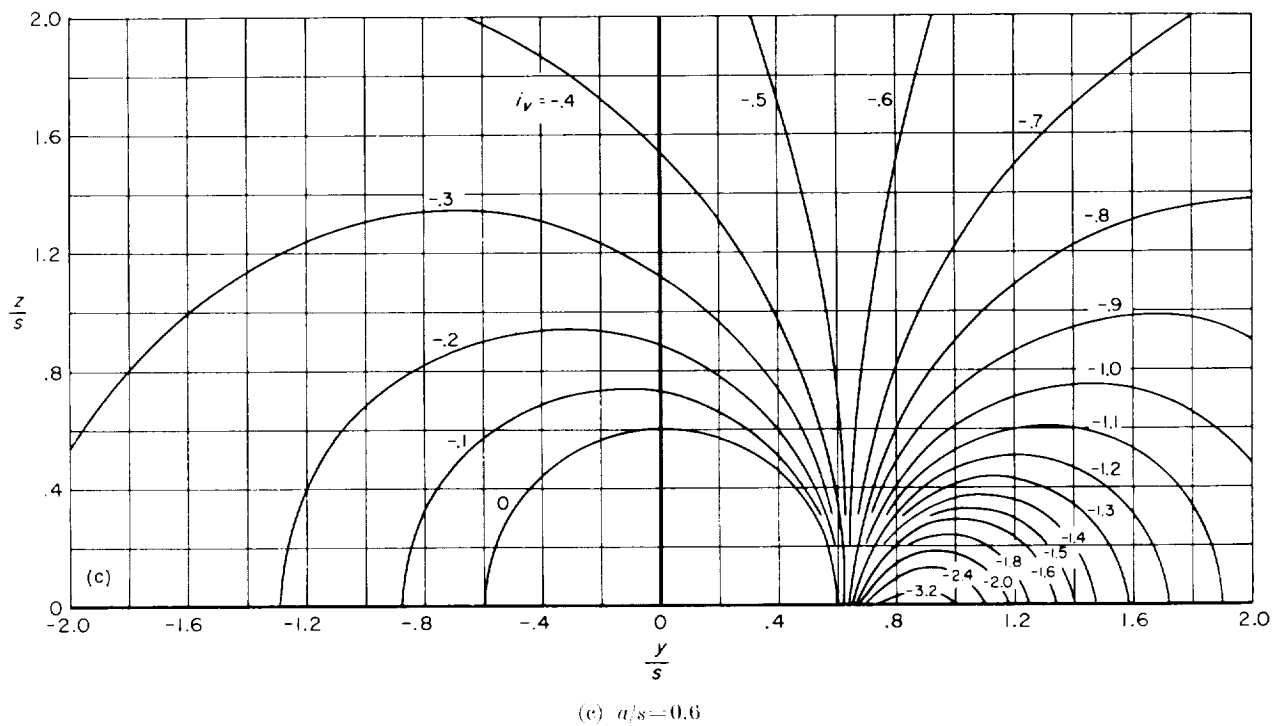


FIGURE 4. Concluded.

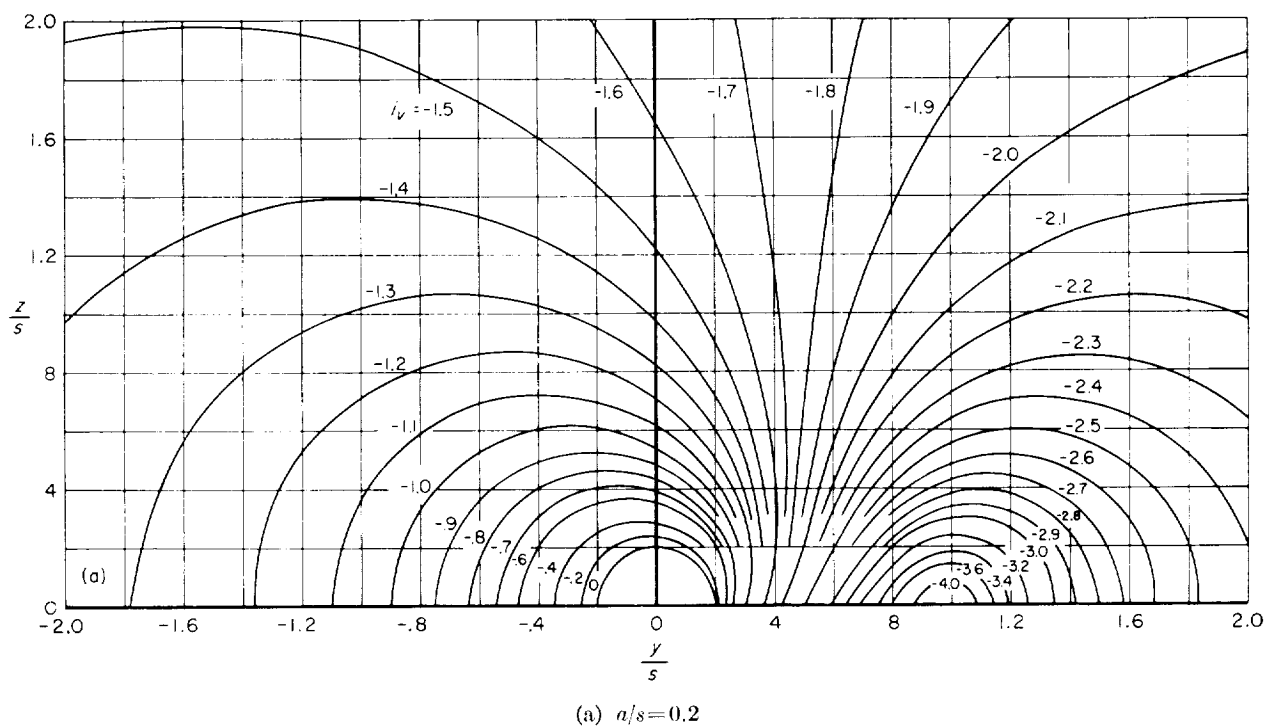


FIGURE 5.—Vortex-interference factors for a linear span load distribution with a root to tip load ratio of 2.

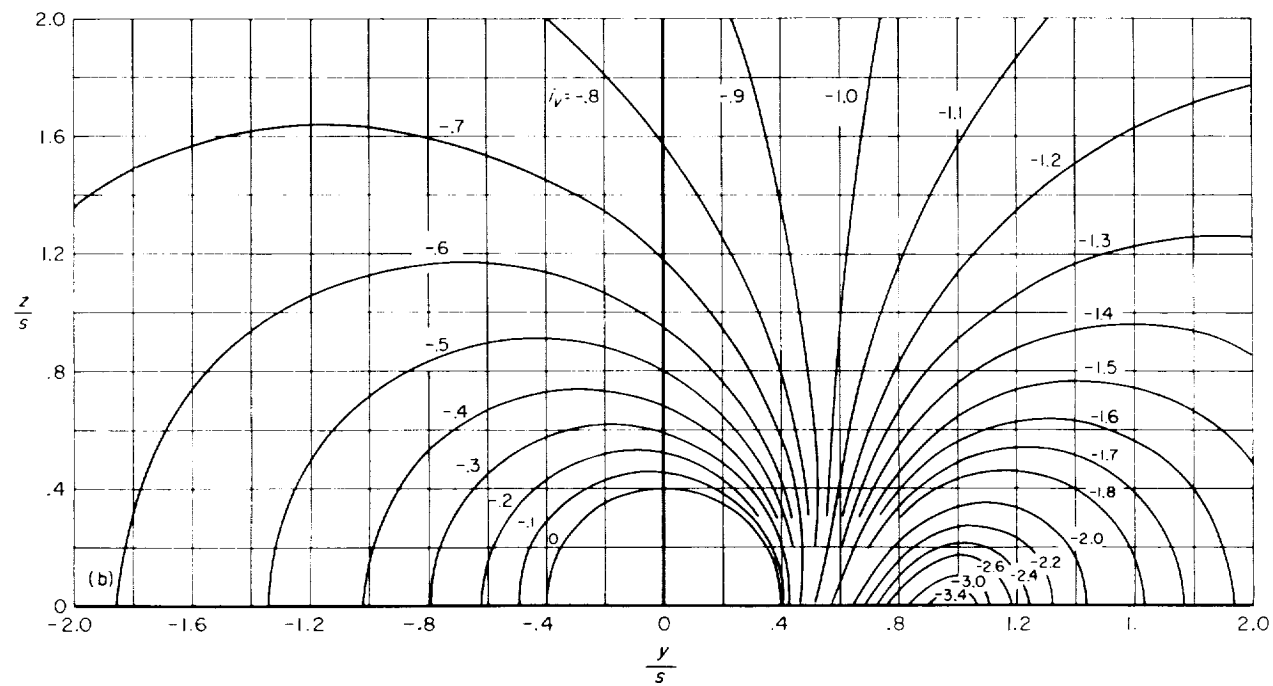


FIGURE 5. --Continued.

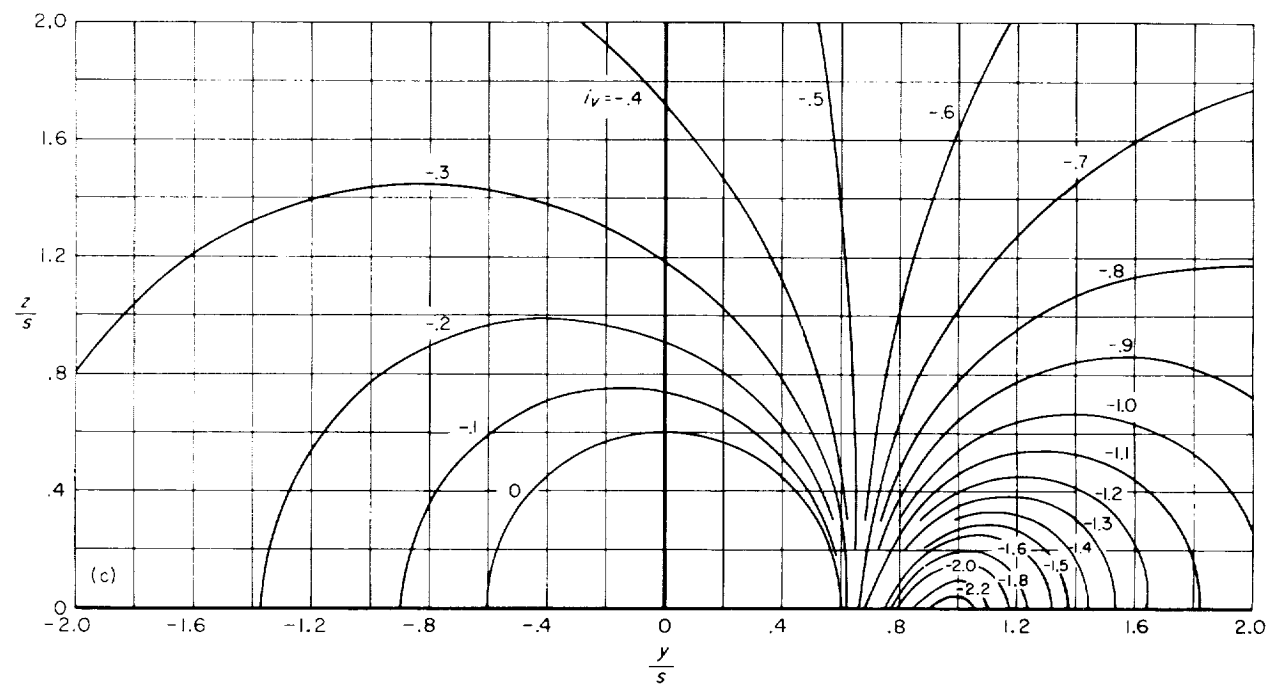


FIGURE 5. --Concluded.

calculation of the paths of a vortex pair in the presence of the family of wing-body combinations shown in figure 2(a), and also to the calculation of the corresponding load distributions, forces, and moments induced by the vortices on these combinations. For these calculations the vortex strength and initial positions (at $x=0$) as well as the configuration orientation to the stream are specified. Hence, the geometry of the forebody is shown unspecified in figure 2(a). The table presented in figure 2(a) lists the parameters which were varied independently over the range indicated while the remaining quantities were held constant at the basic values listed.

Evaluation of the theoretical method was made by means of comparisons of computed vortex paths, forces, and moments with experimental results for the three specific configurations shown in figures 2 (b), (c), and (d) and with the results computed by two alternate theoretical methods. The experimental results for configuration B were obtained from reference 1; those for configuration C, from unpublished wind-tunnel tests; and those for configuration D, from reference 17. The method used to extract the experimental forces and moments due to vortex-interference effects depended upon the nature of the available data. In the case of configuration B, where only wing-panel forces and moments were measured, the effects of the forebody vortices on the normal force and pitching moment were calculated from the relationships

$$C'_{N_v} = \frac{K_w}{k_w} (C'_{N_{W(B)}} - C'_{N_{W, \varphi=0}} K_w \cos \varphi) \quad (45)$$

$$C'_{m_v} = \frac{K_w}{k_w} (C'_{m_{W(B)}} - C'_{m_{W, \varphi=0}} K_w \cos \varphi) \quad (46)$$

where all of the aerodynamic coefficients were obtained from experimental results. The wing-body interference lift ratios K_w and k_w given by slender-body theory were obtained from reference 2 in which it was shown by comparisons with experiment that these ratios are valid for combinations having arbitrary wing plan forms at either subsonic or supersonic speed. This result confirms the observation made in reference 18 that the theoretical lift ratios apply to any wing-body combination having a cylindrical body

and a spanwise load distribution corresponding to minimum vortex drag. The total forces and moments acting on the winged portion of the combination are given by

$$C'_N = \frac{K_w}{k_w} C'_{N_{W(B)}} \quad (47)$$

$$C'_m = \frac{K_w}{k_w} C'_{m_{W(B)}} \quad (48)$$

In the cases of configurations C and D where the forces and moments have been measured on the bodies in various combinations with the wings and canard surfaces, the normal force and pitching moment induced by the canard-surface vortices on the wing-body combinations were determined from the relationships

$$C'_{N_v} = C'_{N_{BWC}} - C'_{N_{BC}} - C'_{N_{BW}} + C'_{N_B} \quad (49)$$

$$C'_{m_v} = C'_{m_{BWC}} - C'_{m_{BC}} - C'_{m_{BW}} + C'_{m_B} \quad (50)$$

In the comparisons between the calculated and experimental forces and moments, the slender-body method of the present investigation is designated "(1) curved paths, slender-body forces." The two alternate methods are called "(2) straight paths, slender-body forces" in which the vortex paths are assumed parallel to the body axis and the forces and moments are computed by the slender-body theory of (1); and "(3) straight paths, reverse-flow forces," in which the vortex paths are the same as those for (2) and the forces and moments are calculated by the linear-theory method. The vortex strengths and initial positions used to calculate the vortex paths and induced loads are listed in table II.

The results of these calculations and comparisons with experiment are discussed in the following paragraphs. The calculated vortex paths, as affected by the parameters of figure 2(a), are first considered and are then compared with observed vortex paths. The corresponding load distributions, forces, and moments due to vortices are then discussed, and finally the comparisons are shown between the calculated and measured forces and moments acting on configurations B, C, and D.

VORTEX PATHS

The calculated paths for configuration A (fig. 2(a)) are presented in figures 6 to 11 in terms of the vortex locations in the transverse (y - z) plane at the indicated longitudinal positions, x/a . The corresponding locations of the local leading edges of the wing panels are also shown on these figures for convenience in relating the vortex paths to the wing-body geometry. Comparisons of the calculated vortex paths with experimentally observed positions for configurations C and D are presented in figures 12 and 13.

Vortices of various strengths.—Figure 6 is presented to show the influence on the vortex motions of changes in the vortex strength. Since the angle of pitch, initial vortex position, and wing geometry are fixed, this variation in vortex strength might represent, for example, the effects of changes in incidence of canard surfaces mounted ahead of

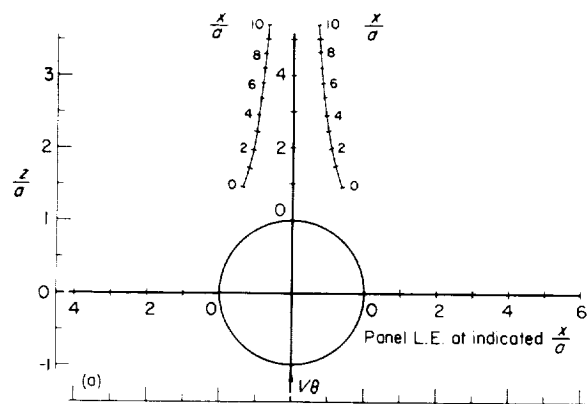
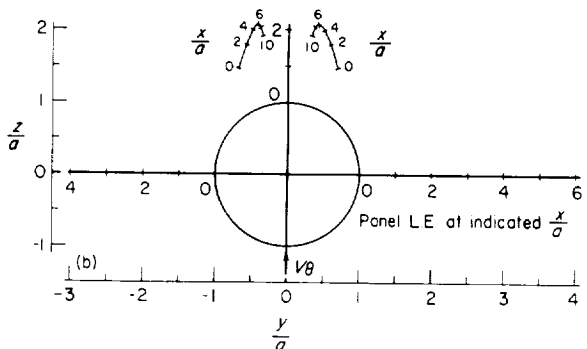
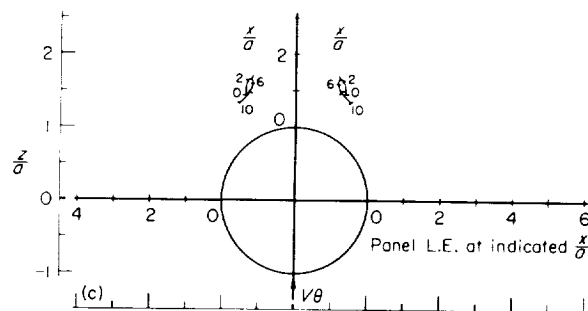
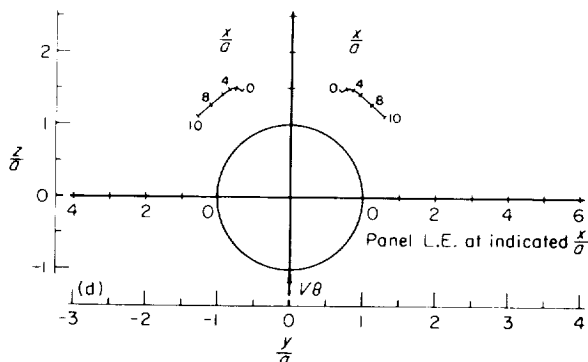
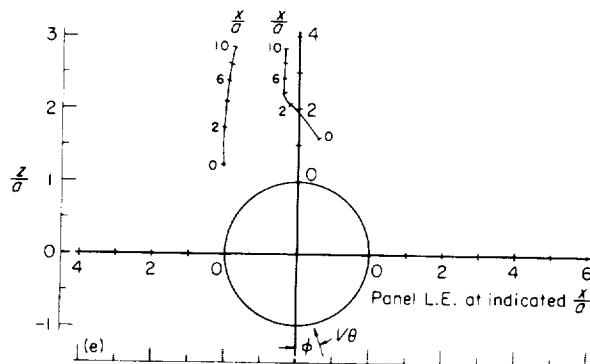
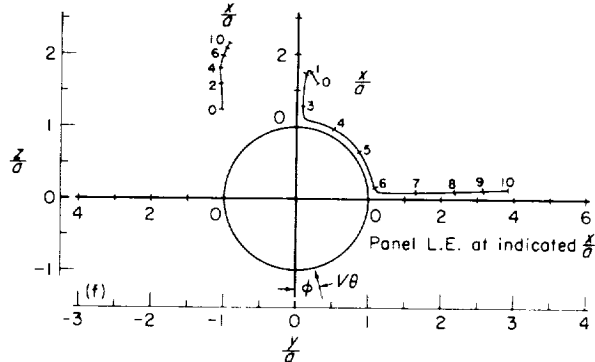
(a) $C_L = 0$; $\varphi = 0^\circ$; $\rho_1 = 65^\circ$ (b) $C_L = 0.132$; $\varphi = 0^\circ$; $\rho_1 = 65^\circ$ (c) $C_L = 0.263$; $\varphi = 0^\circ$; $\rho_1 = 65^\circ$ (d) $C_L = 0.395$; $\varphi = 0^\circ$; $\rho_1 = 65^\circ$ (e) $C_L = 0$; $\varphi = 15^\circ$; $\rho_1 = 80^\circ$ (f) $C_L = 0.132$; $\varphi = 15^\circ$; $\rho_1 = 80^\circ$

FIGURE 6.—Vortex paths for various vortex strengths; configuration A with cruciform wing; $\theta = 20^\circ$; $A = 2$.

FIGURE 6.—Continued.

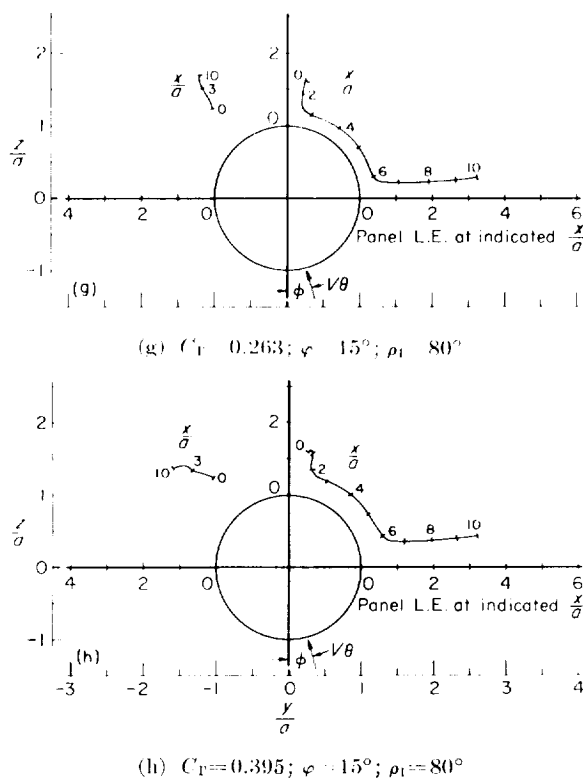


FIGURE 6.—Concluded.

the wing. The vortex paths given in figures 6 (a) and (e) for a vortex strength of 0 represent streamlines of the potential crossflow. It is noted that as the vortex strength increases, the vortex motions in the direction of the potential streamlines decrease and reversals in the paths occur earlier. These results are caused primarily by an increase in the mutual effects of the velocities induced by the vortices and their image systems due to an increase in vortex strength. For most of the vortex paths shown in figure 6, these vortex-induced velocities acted in a direction counter to the potential crossflow.

Vortices of various initial positions. To show the effects of changes in the initial distance between two vortices of constant strength on their subsequent paths, figure 7 is presented. The curves show that as the initial distance is diminished, the succeeding vortex motions increase, and an earlier reversal in the direction of the paths occurs in those cases where such reversal takes place. These changes are the results of increases in the mutual induction among the vortices and their images in accordance with the fundamental

relationship that the velocity induced by one vortex at the location of another is inversely proportional to the distance between the two vortices.

Angles of roll. To show how the vortex paths are influenced by the proximity of the vortices to the wing panel, the paths are presented in figure 8 for the cruciform configuration at various roll angles. It is noted that in all cases the vortices initially move in the direction of potential-flow streamlines (fig. 6 (a) and (e)) but that in many cases the direction of these paths is reversed, resulting in a motion counter to the potential-flow streamlines, for example, the right-hand vortex path of figure 8(a). It is also observed that the closer a vortex is to the surface of the body or a wing panel as the result of a change in the angle of roll, the more rapid is the vortex motion (see, e.g., figs. 8 (a) to (e)). These results stem from the fact that the motion of a vortex is influenced by two factors: (1) the potential crossflow and (2) the vortex flow, consisting of the flow due to the other vortex, the image vortices inside the wing-body combination, and the reaction from the body or wing panel on the vortex due to the effect of this vortex. In those cases where a vortex passed close to a wing or body it moved close to its image vortex in the mathematical model and, hence, the effect of the image vortex predominates over all other effects. For example, the paths of the right-hand vortex for roll angles of 15° to 30° (figs. 8 (c), (d), and (e)) can be explained qualitatively on this basis. In these cases, the reversal in the direction of the vortex path is caused by the influence of the upper vertical wing panel which comes close to the vortex when x/a exceeds 1. This effect is represented in the calculations by an image vortex inside the wing panel and directly opposite the external vortex. The image vortex rotates in a clockwise direction, and thus imparts a downward motion to the external vortex when it is on the right-hand side of the wing panel and an upward motion when on the left-hand side. When the external vortex approaches the wing leading edge the image carries the vortex around the edge from one side to the other; this effect can be seen for a roll angle of 30° (fig. 8(e)). It is noted that the motion of the vortex beside the vertical wing panel is continued along the body and the right horizontal wing until the vortex moves away from the surface, in which

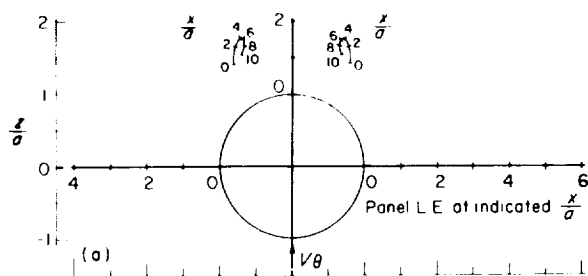
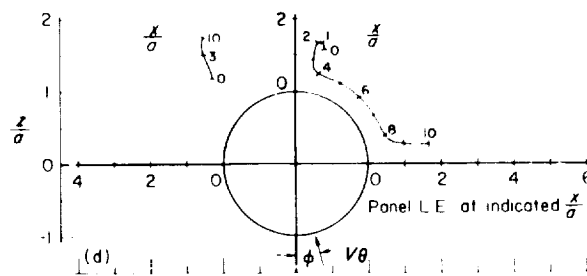
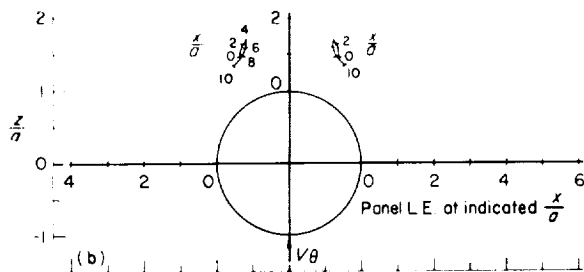
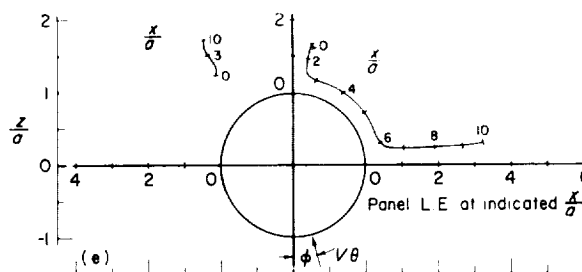
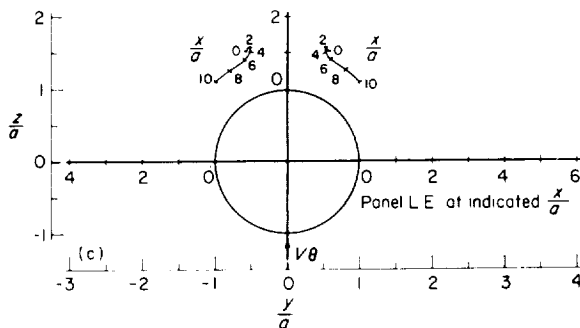
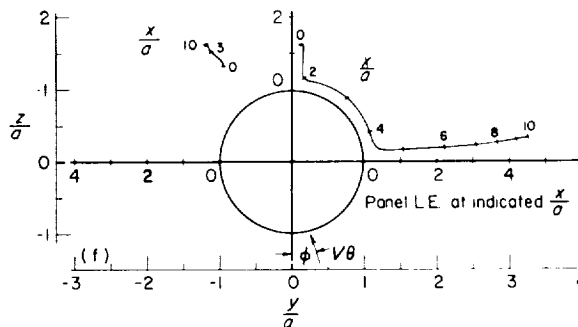
(a) $\rho_1 = 60^\circ; \varphi = 0^\circ$ (d) $\rho_1 = 75^\circ; \varphi = 15^\circ$ (b) $\rho_1 = 65^\circ; \varphi = 0^\circ$ (e) $\rho_1 = 80^\circ; \varphi = 15^\circ$ (c) $\rho_1 = 70^\circ; \varphi = 0^\circ$ (f) $\rho_1 = 85^\circ; \varphi = 15^\circ$

FIGURE 7.--Vortex paths for various initial vortex positions; configuration A with cruciform wing; $\theta = 20^\circ$; $A = 2$; $C_r = 0.263$.

case the influence of the image vortex decreases and the vortex follows a path approaching a potential-flow streamline. It is observed from figure 8 that a critical roll angle exists for this example between 30° and $33\frac{3}{4}^\circ$ which determines whether the vortex is sufficiently close to the wing to be turned around the leading edge or to remain on the left-hand side.

The calculated vortex paths for a planar-wing and body combination are presented in figure 9. The large effect of the vertical wing panels on the

vortex paths when the configuration is at an angle of roll is evident from a comparison of this figure with figure 8 for a given roll angle.

Angles of pitch.---Figure 10 is presented to show the effects of pitch angle in changing the motions of vortices having fixed initial positions. Since the inclination of a body results in a proportional increase in the strength of the shed vorticity, the vortex strength for the present calculations was accordingly increased in direct proportion to the pitch angle. The results of figure 10 show that

FIGURE 7.--Concluded.

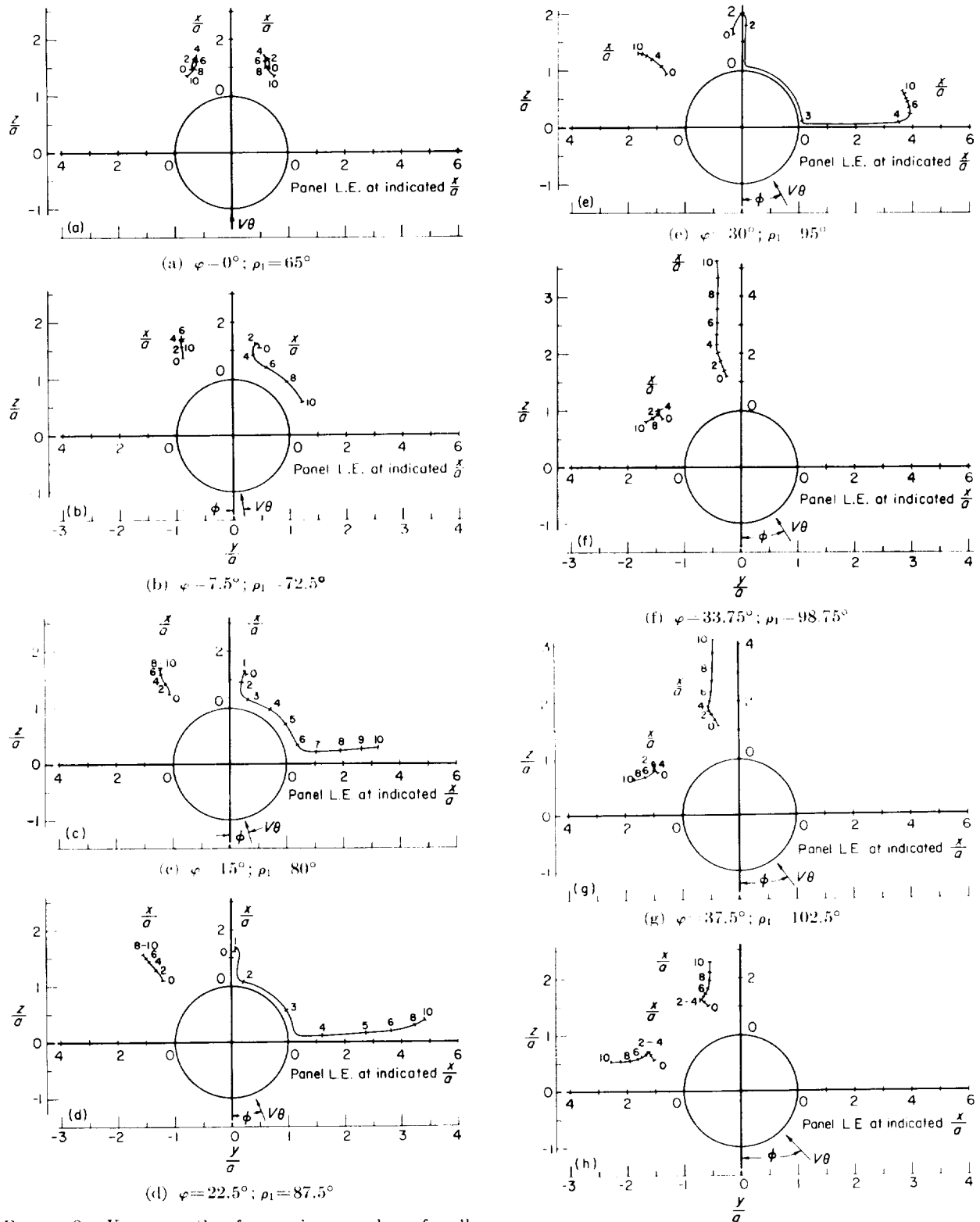


FIGURE 8.—Vortex paths for various angles of roll; configuration A with cruciform wing; $\theta = 20^\circ$; $A = 2$; $C_F = 0.263$.

FIGURE 8.—Concluded.

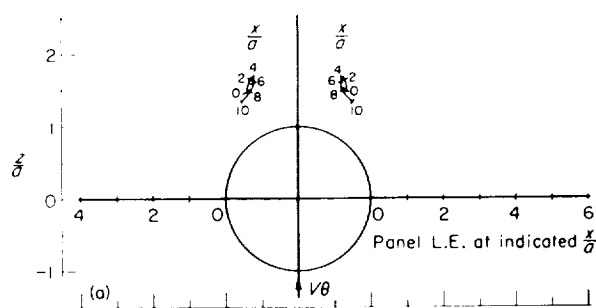
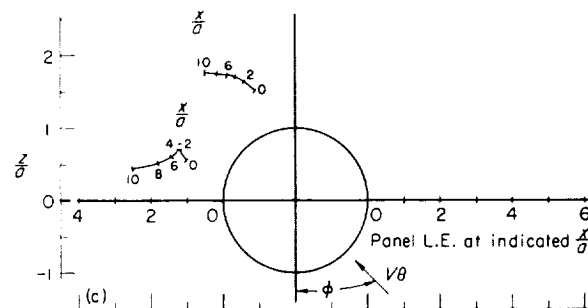
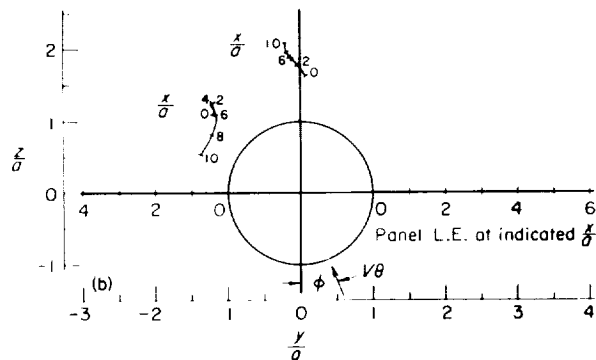
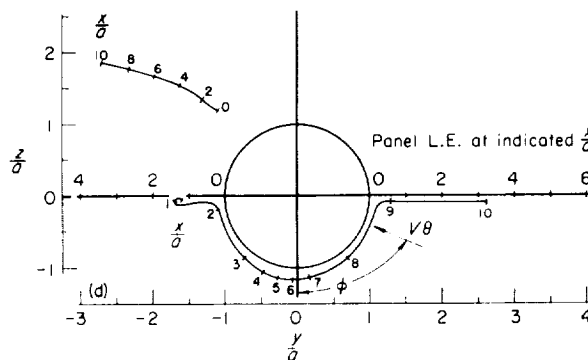
(a) $\varphi = 0^\circ$; $\rho_1 = 6.5^\circ$ (c) $\varphi = 15^\circ$; $\rho_1 = 110^\circ$ (b) $\varphi = 22.5^\circ$; $\rho_1 = 87.5^\circ$ (d) $\varphi = 67.5^\circ$; $\rho_1 = 132.5^\circ$ FIGURE 9. Vortex paths for various angles of roll; configuration A with planar wing; $\theta = 20^\circ$; $A = 2$; $C_F = 0.263$.

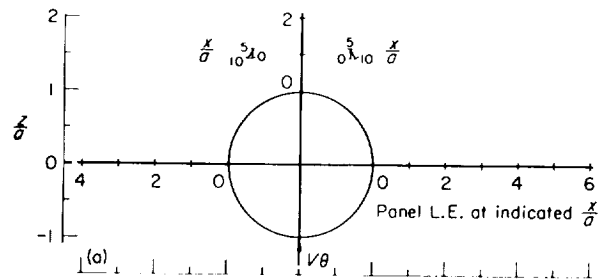
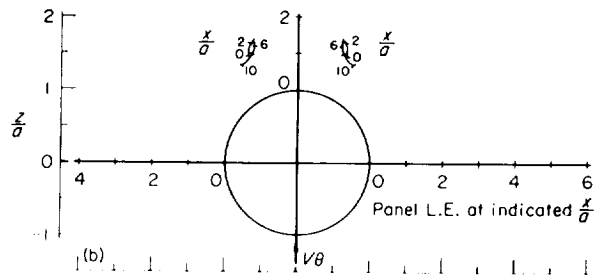
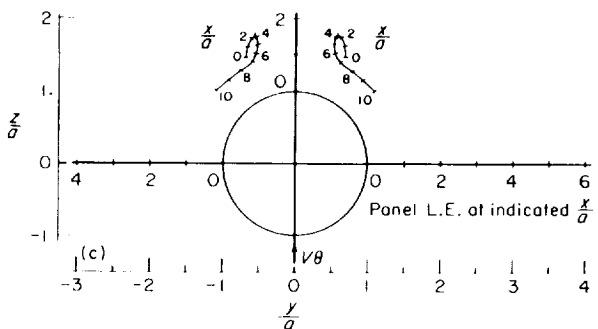
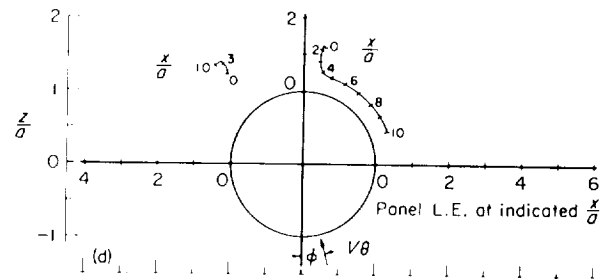
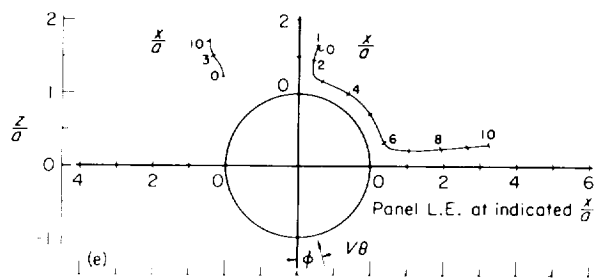
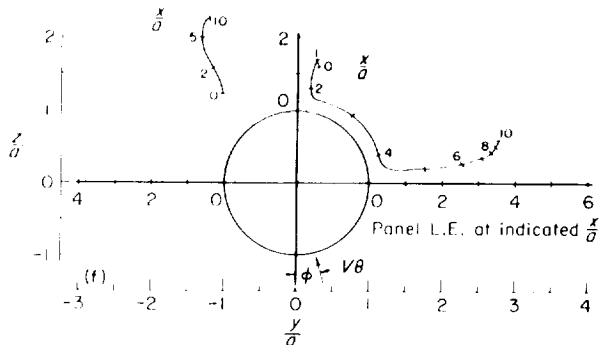
FIGURE 9. Concluded.

these changes in angle of pitch and vortex strength caused an increase in the vortex motions for both roll angles. This increase would be expected since the velocities due to both the potential crossflow and the vortex flow are increased when the angle of pitch and vortex strength are increased. The increasing downward movement in the vortices at $\varphi = 0$ and in the right-hand vortex at $\varphi = 15^\circ$ due to an increase in pitch angle indicates that the motions of these vortices are influenced primarily by the increase in vortex strength, whereas the corresponding increasing upward movement of the left-hand vortex at $\varphi = 15^\circ$ shows that the motion of this vortex is influenced mainly by the increase in the potential crossflow velocities caused by the increased inclination of the body.

Wings of various aspect ratios. In order to show the change of vortex motions due to an increase in the wing span relative to the body diameter, vortex paths are presented in figure 11 for various wing aspect ratios. Since the angle of attack and vortex strength are constant, the vortex paths are influenced by only two effects: (1)

change in the potential crossflow field due to the wing panels and (2) change in the vortex image system of the wing panels. At $\varphi = 0$, an increase in the aspect ratio causes a change in the crossflow which moves the two vortices closer together initially, and this, in turn, increases the mutual downward induction between the vortices. Thus, as the aspect ratio is increased the reversal in the vortex motion occurs earlier. At a roll angle of 15° , the primary effect of wing aspect ratio is upon the vortex image system of the wing panels which influences the vortex paths. The upper wing panel controls the reversal in the path of the right-hand vortex and the right horizontal panel influences primarily the lateral motion of this vortex.

Comparisons of calculated and measured vortex paths.—To evaluate the calculative method for predicting vortex paths in some specific cases, comparisons are presented in figures 12 and 13 between some observed vortex paths and the paths computed by the slender-body method. Figure 12 shows that the path of the observed vortex

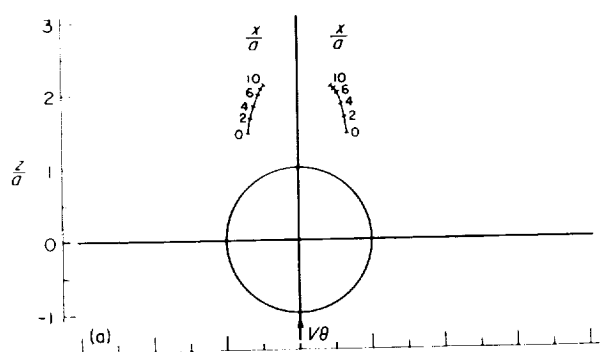
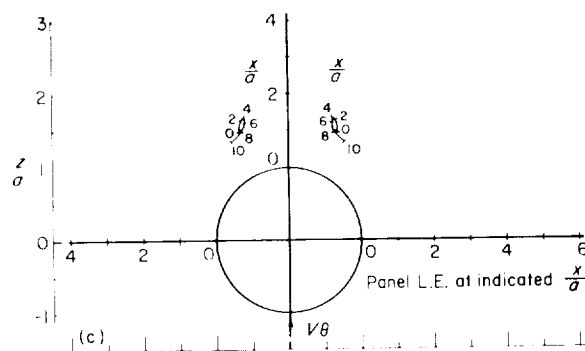
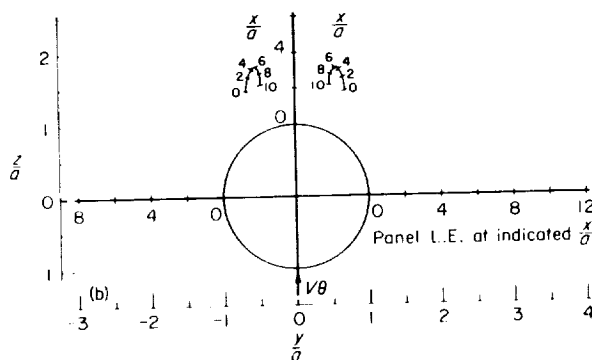
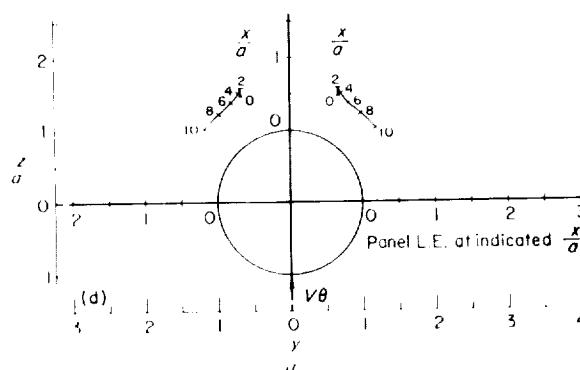
(a) $\theta = 10^\circ$; $C_L = 0.132$; $\varphi = 0^\circ$; $\rho_L = 65^\circ$ (b) $\theta = 20^\circ$; $C_L = 0.263$; $\varphi = 0^\circ$; $\rho_L = 65^\circ$ (c) $\theta = 30^\circ$; $C_L = 0.395$; $\varphi = 0^\circ$; $\rho_L = 65^\circ$ (d) $\theta = 10^\circ$; $C_L = 0.132$; $\varphi = 15^\circ$; $\rho_L = 80^\circ$ (e) $\theta = 20^\circ$; $C_L = 0.263$; $\varphi = 15^\circ$; $\rho_L = 80^\circ$ (f) $\theta = 30^\circ$; $C_L = 0.395$; $\varphi = 15^\circ$; $\rho_L = 80^\circ$ FIGURE 10.—Calculated vortex paths for various pitch angles; configuration A with cruciform wing; $A=2$.

core over most of the wing of configuration C is in reasonably close agreement with the calculated path. The difference between the calculated and experimental lateral positions at the forward part of the wing stems from the fact that the observed vortex core represents only the rolled-up portion of the trailing vortex wake, and thus is located outboard of the computed vortex which is located at the center of gravity of the total vorticity. As the wake travels downstream it tends to become increasingly rolled up into a single vortex repre-

FIGURE 10. Concluded.

sented by the observed vortex core. Because the observed core tends to approach the calculated path, this path is considered to be a close prediction of the center of gravity of the actual vortex wake. These results are in basic agreement with those obtained in reference 19 for wings in incompressible flow.

Figure 13 indicates that the trends in the vortex paths of configuration D are predicted by the calculated results but that in many cases the actual vortex positions are considerably different from the

(a) $A=0$; $\varphi=0^\circ$; $\rho_1=65^\circ$ (c) $A=2$; $\varphi=0^\circ$; $\rho_1=65^\circ$ (b) $A=1$; $\varphi=0^\circ$; $\rho_1=65^\circ$ (d) $A=4$; $\varphi=0^\circ$; $\rho_1=65^\circ$ FIGURE 11.—Vortex paths for various wing aspect ratios; configuration A with cruciform wing; $\theta=20^\circ$; $C_L=0.263$.

predicted positions. These differences are believed to be the result of three-dimensional effects associated with the nonslender effective aspect ratio BA of the wing which is about 1.7 at $M=1.3$ and 4.0 at $M=2.2$. Since the calculative method is based on slender-body theory, it would be expected to predict accurately the vortex path only for combinations having wings of low effective aspect ratio, such as configuration C which has a value of about 1.0 at a Mach number of 3.0.

LOAD DISTRIBUTIONS, FORCES, AND MOMENTS DUE TO VORTICES

Calculated load distributions, forces, and moments acting on configuration A due to a pair of vortices following the calculated paths previously discussed are given in figures 14 to 21. The force curves may also be used to calculate the longitudinal load distributions since

$$\frac{dC'_N}{dx} = \frac{1}{\pi} \int_{-1}^1 \left(\frac{\Delta p}{q} \right)_N \frac{dy}{s}$$

and

$$\frac{dC'_Y}{dx} = \frac{1}{\pi} \int_{-1}^1 \left(\frac{\Delta p}{q} \right)_Y \frac{dy}{s}$$

Thus, the slope of a force curve at a given value of x/a represents the total induced load at that longitudinal position.

Comparisons of the calculated forces and moments with experimental results for configurations B, C, and D (fig. 2) are given in figures 22 to 29.

Vortices of various strengths. The vortex-induced forces and moments for several vortex strengths are presented in figure 14, corresponding to the vortex paths of figure 6. It is noted that

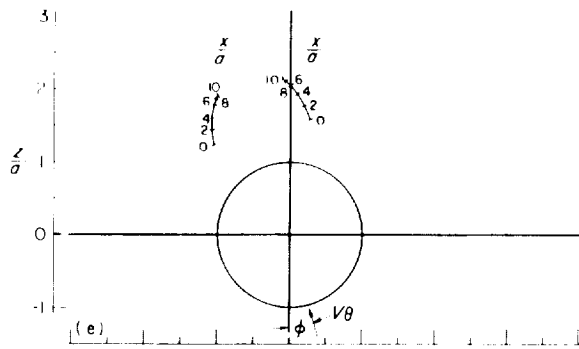
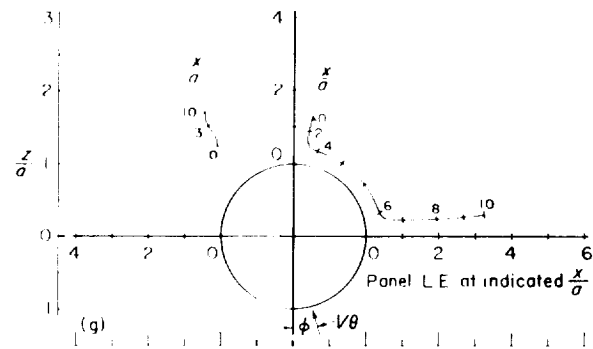
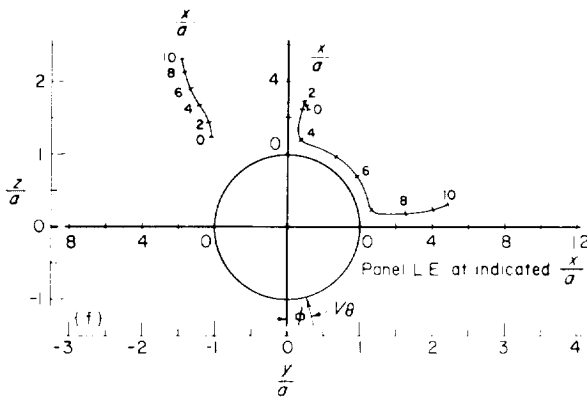
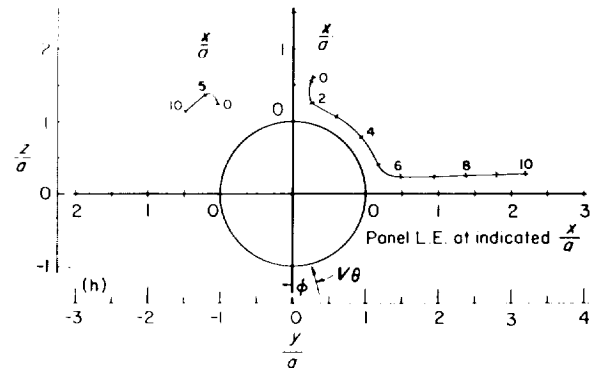
(e) $A = 1$; $\varphi = 15^\circ$; $\rho_1 = 80^\circ$ (g) $A = 2$; $\varphi = 15^\circ$; $\rho_1 = 80^\circ$ (f) $A = 1$; $\varphi = 15^\circ$; $\rho_1 = 80^\circ$ (h) $A = 4$; $\varphi = 15^\circ$; $\rho_1 = 80^\circ$

FIGURE 11.—Continued.

FIGURE 11.—Concluded.

in some cases an increase in vortex strength results in a proportional increase in the induced forces and moments. The deviation from this result for the remaining cases reflects the influence of changes in the vortex paths due to changes in the vortex strength.

Vortices of various initial positions.—The vortex-induced forces and moments for various initial vortex positions are presented in figure 15, corresponding to the vortex paths of figure 8. It is noted that in general the induced forces and moments are smaller since the two vortices start closer together (larger ρ_1) but that differences in the subsequent paths of these vortices exert a strong influence on the forces and moments.

Angles of roll.—The spanwise load distributions due to vortices, corresponding to the vortex paths of figure 8, are shown in figure 16. A comparison

of these two figures for a given roll angle illustrates the correspondence of the load distributions with the vortex locations. It is seen that where a vortex is close to the wing or body, large concentrated loads are induced at that point and that on other portions of the configuration the loads are small or negligible.

The vortex-induced forces and moments for various roll angles are shown in figure 17. There is a strong correspondence of these results with the vortex-path results given in figure 8. In those cases where the vortex paths change relatively slowly in the y - z plane, for example, $\varphi = 0^\circ$ and 7.5° , the forces and moments also change rather slowly, but when the paths change rapidly, for example, $\varphi = 22.5^\circ$ and 30° , the forces and moments likewise change rapidly. It can be seen that each change in direction of a vortex path, when close

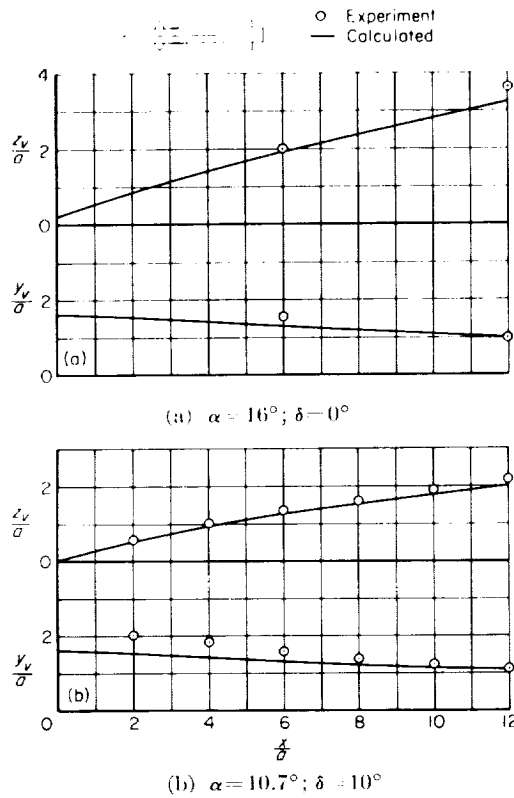


FIGURE 12.—Comparison of calculated and experimental vortex paths; configuration C with inline canard surfaces; $M = 3.0$; $\varphi = 0^\circ$.

to the wing-body combination, results in a corresponding change in the forces and moments. Figure 17 shows that, in general, the vortex-induced forces tend to oppose those acting on the configuration in potential flow. For example, the normal force due to vortices C_{N_v} is negative whereas the total normal force in potential flow is positive at a positive pitch angle. From the slopes of the force curves, it is noted that these opposing loads are located primarily in the region of x/a between 1 and 3 at all roll angles. The center of the vortex load is in all cases ahead of $x/a = 5$ and in some cases ahead of the wing itself (see, e.g., C_{Y_v} and C_{N_v} of fig. 17(b)). This effect is caused by a couple created by opposing loads on the forward and rearward portions of the combination.

The rolling moments induced by the vortices were calculated from integrations of the load

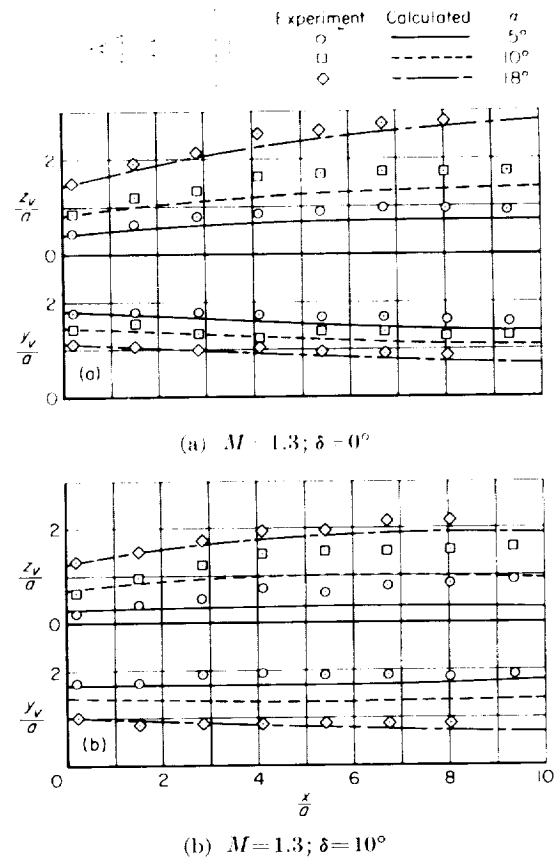


FIGURE 13.—Comparison of calculated and experimental vortex paths; configuration D; $\varphi = 0^\circ$.

distributions, and the results are given in figure 18 for two roll angles. It is noted that for short wing-body combinations (x/a less than about 4) the rolling moments are positive, but for longer combinations they are negative.

The vortex-induced forces and moments for several roll angles of a planar wing-body combination are given in figure 19. Comparison of these results with those for the cruciform configuration (fig. 17) shows that removal of the vertical wing panels causes large changes in the forces which are associated with the changes in vortex paths. Greater maximum induced forces and moments are generally encountered by the planar configuration than the cruciform combination at a given roll angle.

Angles of pitch. The vortex-induced forces and moments for various pitch angles are presented in figure 20. From this figure, it is

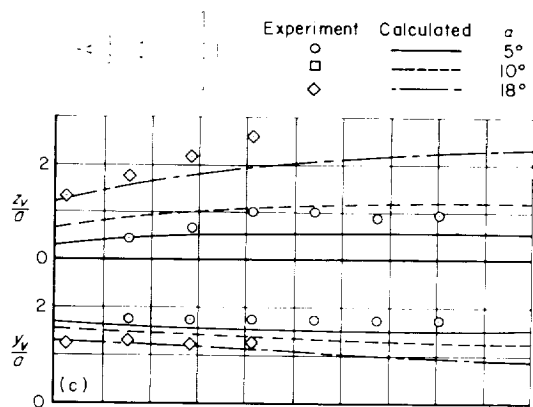
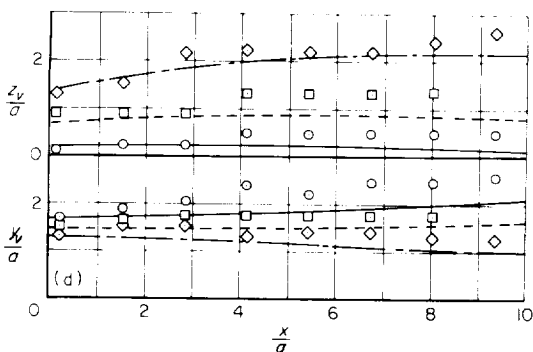
(c) $M=2.2; \delta=0^\circ$ (d) $M=2.2; \delta=10^\circ$

FIGURE 13.—Concluded.

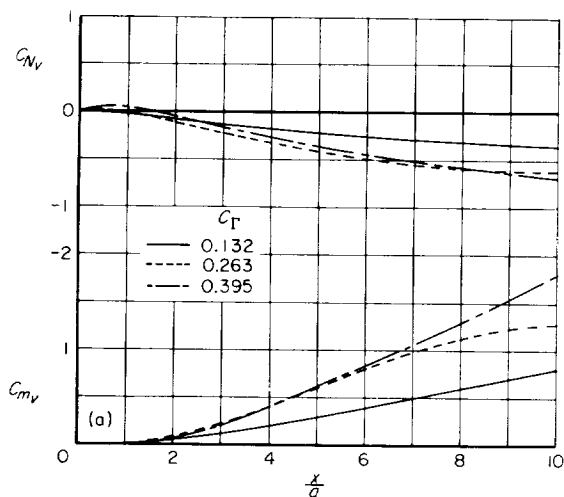
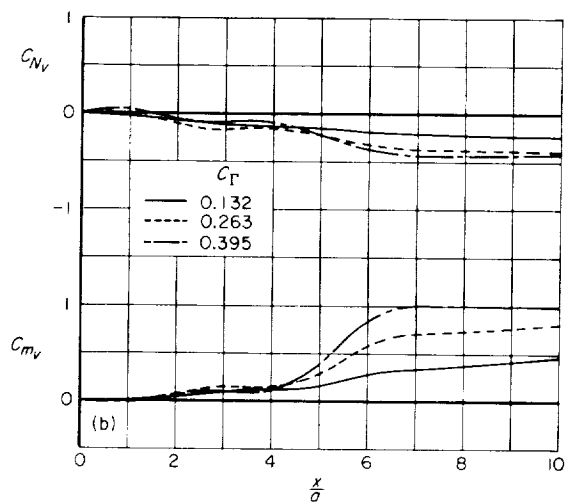
(a) $\varphi=0^\circ; \rho_1=65^\circ$ FIGURE 14.—Effects of vortex strength on forces and moments due to vortices; configuration A with cruciform wing; $\theta=20^\circ$; $A=2$.(b) Longitudinal coefficients; $\varphi=15^\circ; \rho_1=80^\circ$.

FIGURE 14.—Continued.

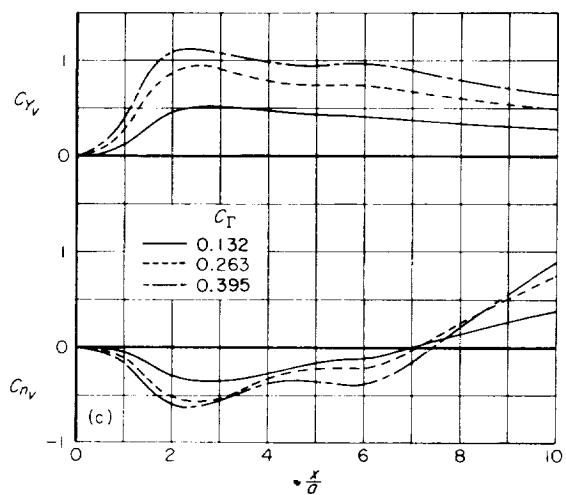
(c) Lateral coefficients; $\varphi=15^\circ; \rho_1=80^\circ$.

FIGURE 14.—Concluded.

apparent that the effects of pitch angle on C_N and C_m at $\varphi=0$ and on C_Y and C_n at $\varphi=15^\circ$ are primarily the result of the corresponding changes in vortex strength because the magnitude of these forces and moments is approximately proportional to the pitch angle. However, the effects of pitch angle on C_N and C_m at $\varphi=15^\circ$ appear to be largely influenced by changes in the vortex paths (fig. 20) because the changes in C_N and C_m are not proportional to pitch angle.

Wings of various aspect ratios.—The vortex-induced forces and moments for various wing

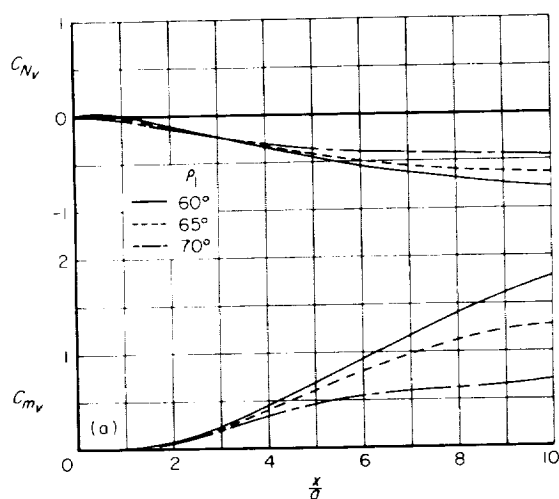
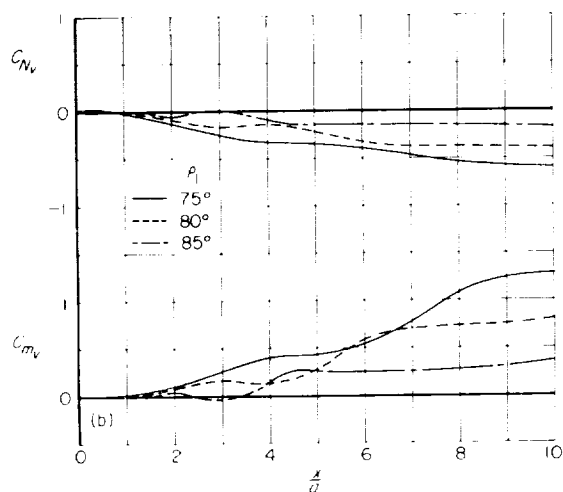
(a) $\varphi = 0^\circ$ FIGURE 15. Effects of initial vortex positions on forces and moments due to vortices; configuration A with cruciform wing; $\theta = 20^\circ$; $A = 2$; $C_T = 0.263$.(b) Longitudinal coefficients; $\varphi = 15^\circ$.

FIGURE 15. Continued.

aspect ratios are presented in figure 21. A change in aspect ratio influences the induced forces and moments on the configuration by changing the vortex paths (fig. 11) and the wing span over which the vortex loading acts. Figure 21 shows that at small values of x/a the forces and moments

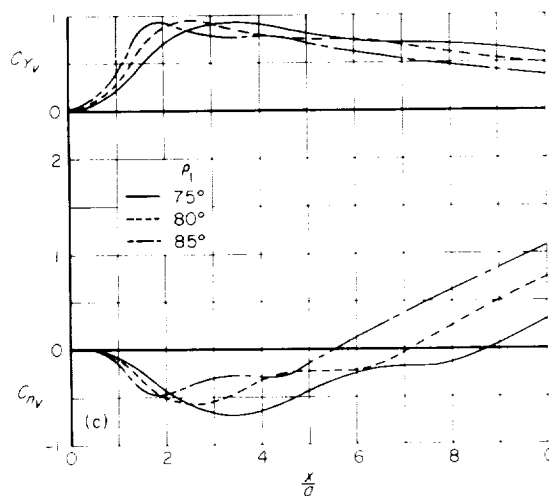
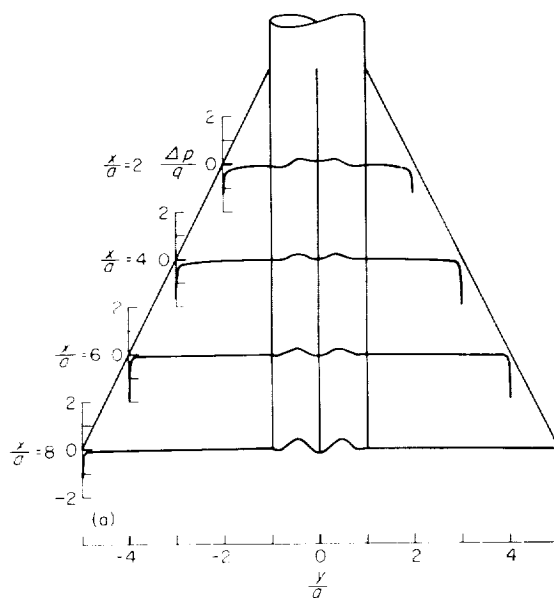
(c) Lateral coefficients; $\varphi = 15^\circ$.

FIGURE 15. Concluded.

(a) $\varphi = 0^\circ$; $\rho_1 = 65^\circ$ FIGURE 16. --Calculated load distribution due to vortices for various angle of roll; configuration A with cruciform wing; $\theta = 20^\circ$; $A = 2$; $C_T = 0.263$.

change progressively with aspect ratio, but at larger values the predominant effects of the vortex paths are evident.

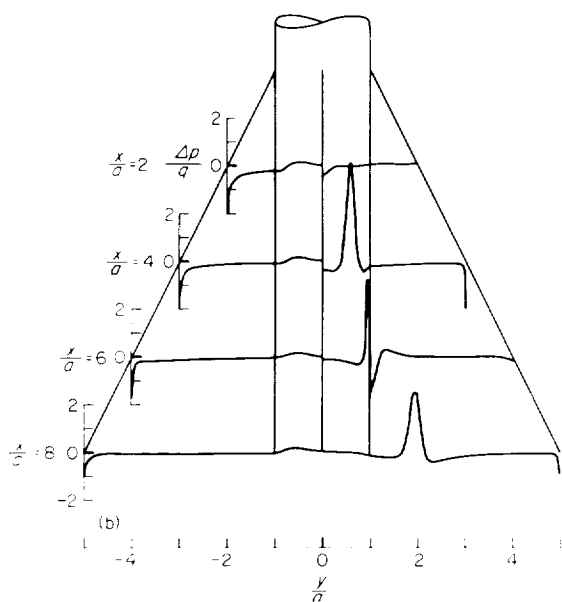
(b) Horizontal surfaces; $\varphi = 15^\circ$; $\rho_1 = 80^\circ$

FIGURE 16.—Continued.

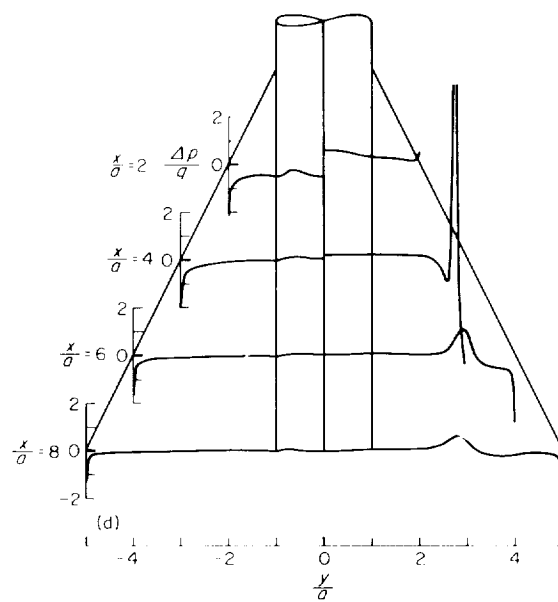
(d) Horizontal surfaces; $\varphi = 30^\circ$; $\rho_1 = 95^\circ$.

FIGURE 16.—Continued.

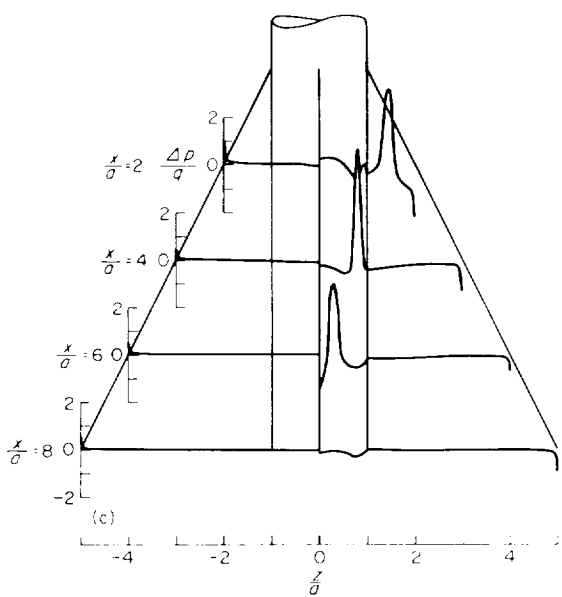
(c) Vertical surfaces; $\varphi = 15^\circ$; $\rho_1 = 80^\circ$

FIGURE 16.—Continued.

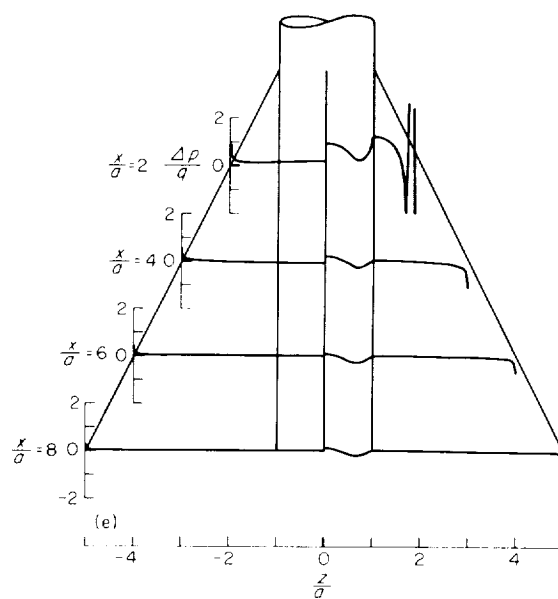
(e) Vertical surfaces; $\varphi = 30^\circ$; $\rho_1 = 95^\circ$.

FIGURE 16.—Continued.

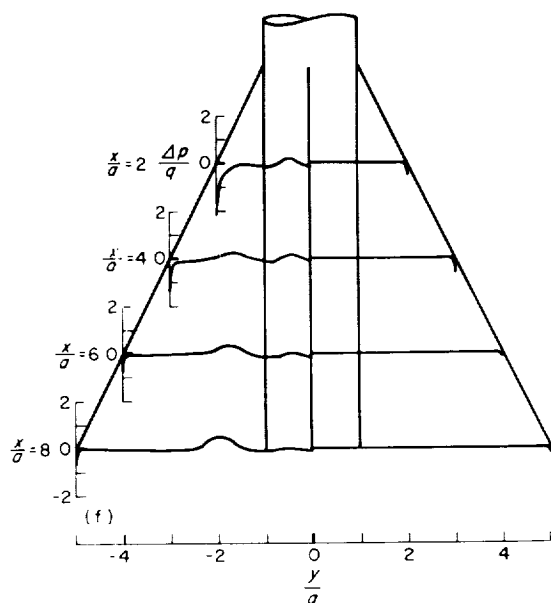
(f) Horizontal surfaces; $\varphi = 45^\circ$; $\rho_1 = 110^\circ$.

FIGURE 16.—Concluded.

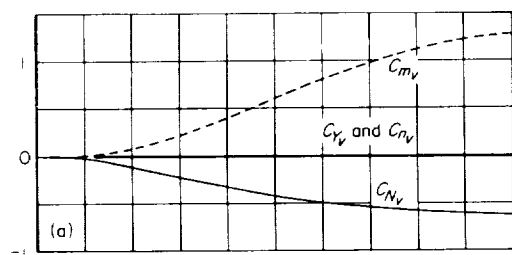
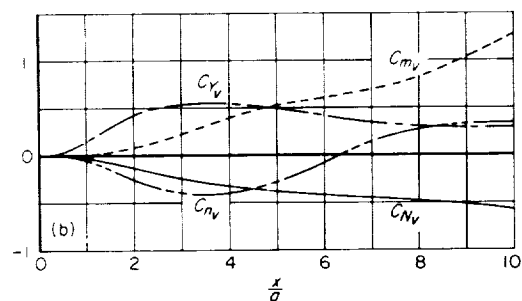
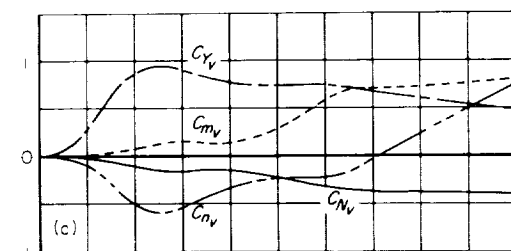
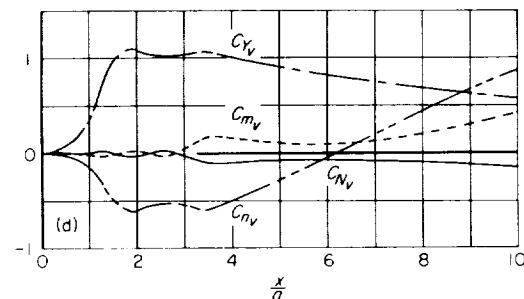
(a) $\varphi = 0^\circ$; $\rho_1 = 65^\circ$ (b) $\varphi = 7.5^\circ$; $\rho_1 = 72.5^\circ$ FIGURE 17.—Forces and moments due to vortices for various angles of roll; configuration A with cruciform wing; $\theta = 20^\circ$; $A = 2$; $C_F = 0.263$.(c) $\varphi = 15^\circ$; $\rho_1 = 80^\circ$ (d) $\varphi = 22.5^\circ$; $\rho_1 = 87.5^\circ$

FIGURE 17.—Continued.

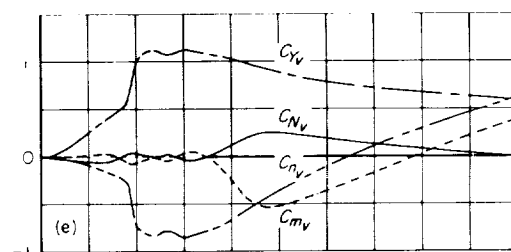
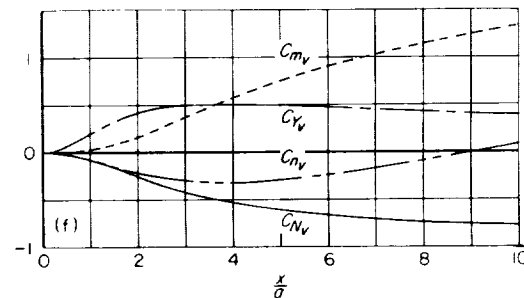
(e) $\varphi = 30^\circ$; $\rho_1 = 95^\circ$ (f) $\varphi = 33.75^\circ$; $\rho_1 = 98.75^\circ$

FIGURE 17.—Continued.

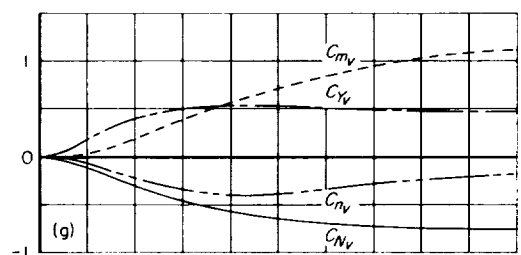
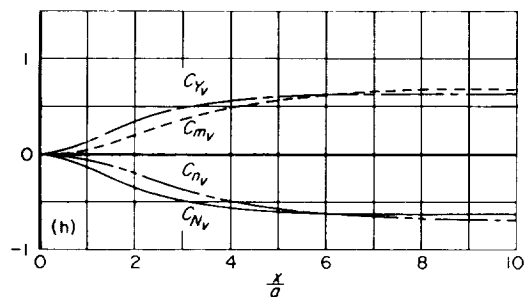
(g) $\varphi = 37.5^\circ$; $\rho_1 = 102.5^\circ$ (h) $\varphi = 45^\circ$; $\rho_1 = 110^\circ$

FIGURE 17.—Concluded.

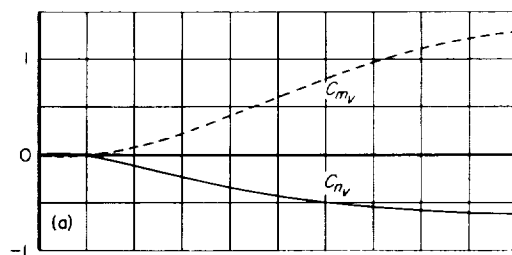
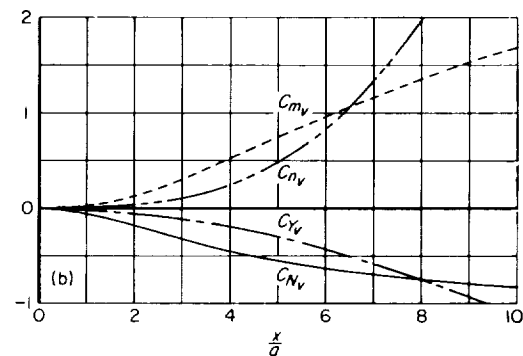
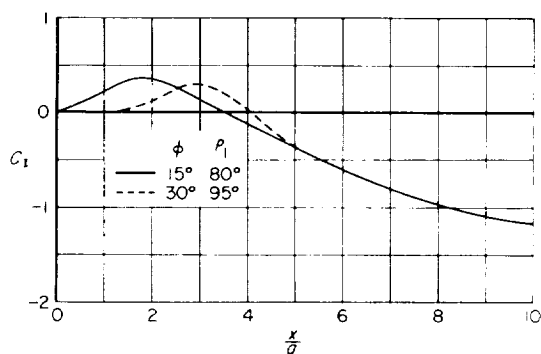
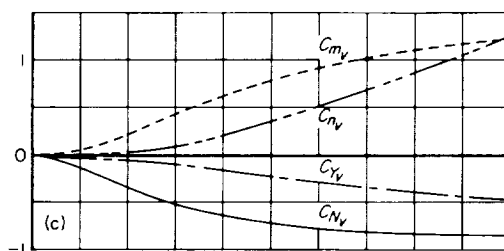
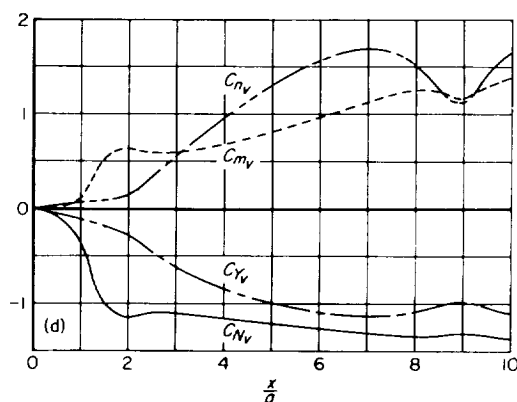
(a) $\varphi = 0^\circ$; $\rho_1 = 65^\circ$ (b) $\varphi = 22.5^\circ$; $\rho_1 = 87.5^\circ$ FIGURE 19.—Forces and moments due to vortices for various angles of roll; configuration A with planar wing; $\theta = 20^\circ$; $A = 2$; $C_T = 0.263$.FIGURE 18.—Effect of roll angle on calculated rolling moment due to vortices; configuration A with cruciform wing; $\theta = 20^\circ$; $A = 2$; $C_T = 0.263$.(c) $\varphi = 45^\circ$; $\rho_1 = 110^\circ$ (d) $\varphi = 67.5^\circ$; $\rho_1 = 132.5^\circ$

FIGURE 19.—Concluded.

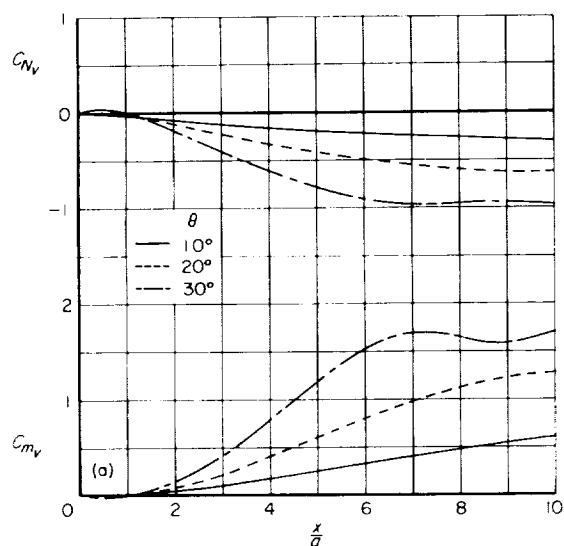
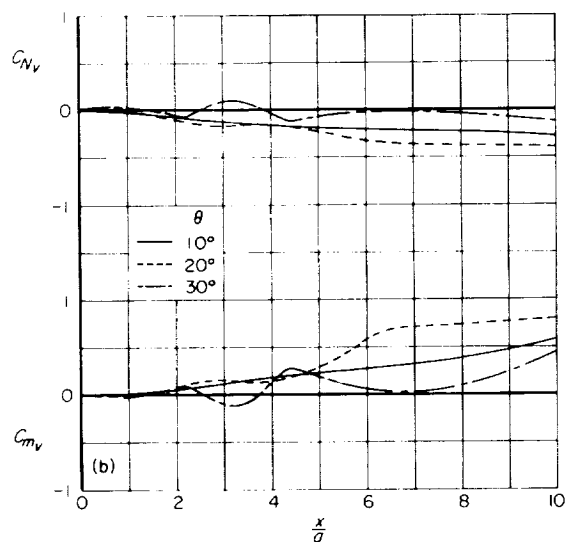
(a) $\varphi=0^\circ$; $\rho_1=65^\circ$ FIGURE 20.—Effects of pitch angle on forces and moments due to vortices; configuration A with cruciform wing; $A=2$; $C_L/\theta=0.0132$ per deg.(b) Longitudinal characteristics; $\varphi=15^\circ$; $\rho_1=80^\circ$.

FIGURE 20.—Continued.

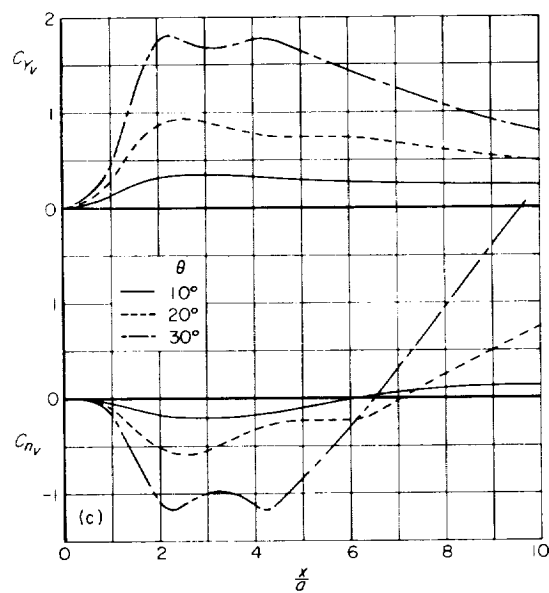
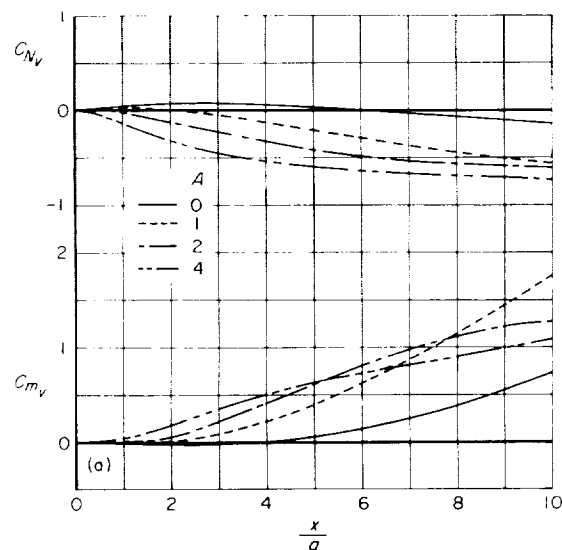
(c) Lateral characteristics; $\varphi=15^\circ$; $\rho_1=80^\circ$.

FIGURE 20.—Concluded.

(a) $\varphi=0^\circ$; $\rho_1=65^\circ$ FIGURE 21.—Effects of wing aspect ratio on forces and moments due to vortices; configuration A with cruciform wing; $\varphi=20^\circ$; $C_L=0.263$.

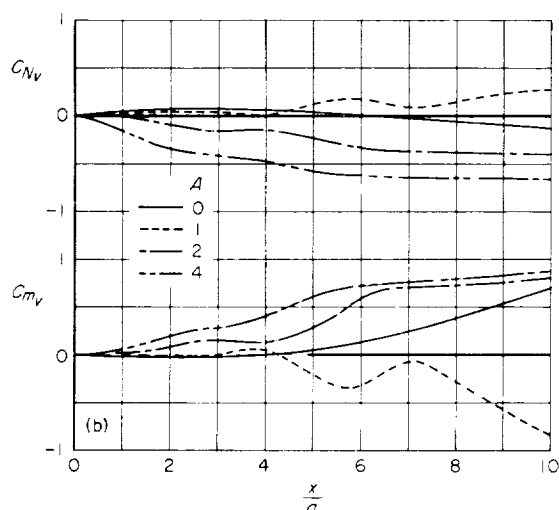
(b) Longitudinal coefficients; $\varphi = 15^\circ$; $\rho_1 = 80^\circ$.

Figure 21.—Continued.

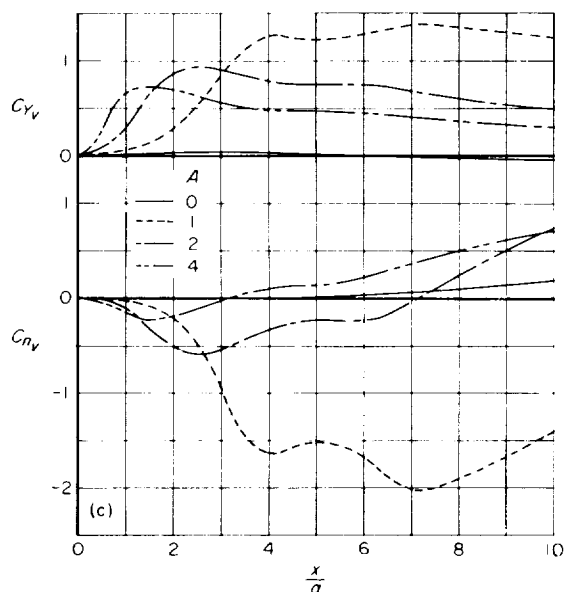
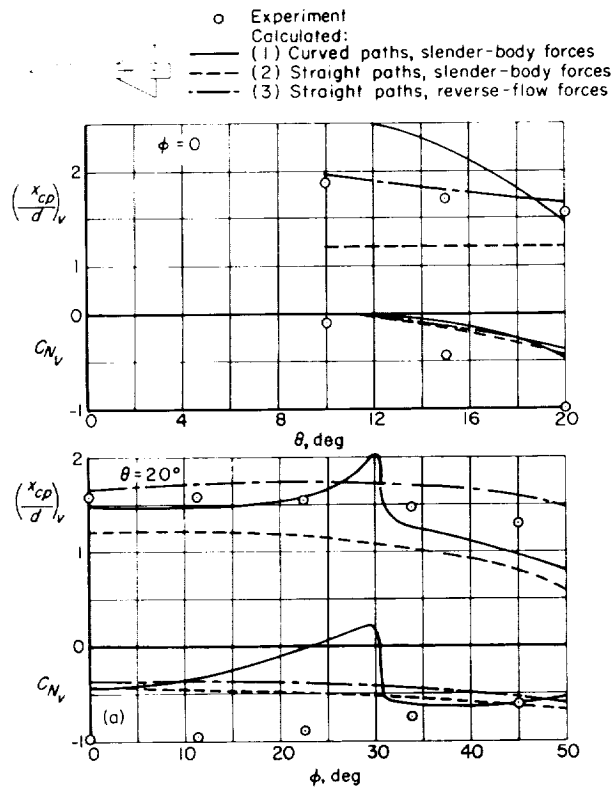
(c) Lateral coefficients; $\varphi = 15^\circ$; $\rho_1 = 80^\circ$.

FIGURE 21.—Concluded.

Comparisons of calculated results with experiment.—Comparisons are presented in figure 22 between the calculated and experimental results for the forces and centers of pressure induced by two forebody vortices on configuration B. These results show that none of the theoretical methods provided a close prediction of the experimental vortex-induced effects over the whole range of pitch and roll angles considered, although for

some conditions the agreement is close. These differences presumably can be attributed to the limitations and assumptions involved in the theoretical methods. Method (1) can be considered to be the most exact in that it takes into account the influence of the wing-body flow field on the vortex paths. However, the methods for calculating the paths and forces are based on slender-body theory and thus are restricted to wing-body combinations having wings of low effective aspect ratio ($BA \ll 4$). Since the effective aspect ratio of the wing of configuration B at a Mach number of 2 is about 3.5 this requirement is not met. Another factor which may prevent the vortices from following the calculated paths is the possible occurrence of regions of flow separation caused by a vortex passing close to the surface. An indication of this effect is shown in figure 22 for the results shown as functions of roll angle φ . The curves calculated by method (1) show abrupt changes at roll angles near 30° , which are the result of one vortex suddenly passing from one side of the upper vertical wing to the other, as discussed previously relative to configuration A (see figs. 8 (e) and (f)). The experimental forces and moments, however, do not show these abrupt changes predicted by the calculated results, indicating that the vortices fail to follow the computed paths at these roll angles. The results for methods (2) and (3) show that the assumption of constant vortex paths (parallel to the body axis) gives variations in the induced forces and moments with roll angle which are closer to the experimental results. These results also show that the use of reverse-flow theory, which takes into account three-dimensional effects, results generally in an improvement in the prediction of the center of pressure of the vortex-induced forces but has little effect on the prediction of the forces themselves.

Comparisons between experimental and calculated results for the total forces and centers of pressure acting on configuration B are presented in figure 23 to show the importance of the differences just discussed for the vortex-induced forces of figure 22. The results indicate that except for roll angles near 25° , the calculated normal force and center of pressure are affected only slightly by the theoretical method used to compute the vortex effects because the vortex-induced normal force is only a small part of the total normal force. The total side force predicted by all three methods

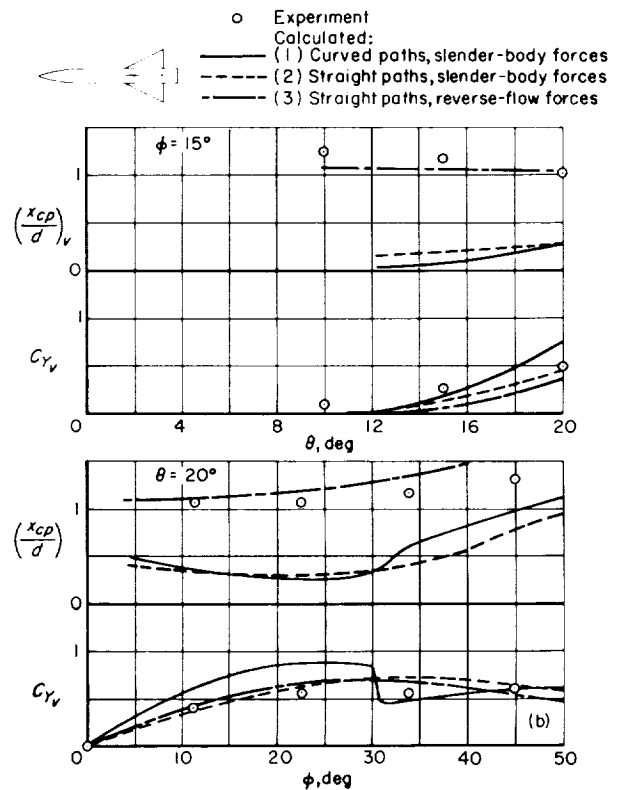


(a) Longitudinal characteristics.

FIGURE 22.—Comparison of calculated and experimental forces and moments due to vortices; configuration B; $M=2.0$.

is in good agreement with experiment but only method (3) was successful in predicting the center of pressure of this force at high pitch angles and low roll angles.

Comparisons between the experimental and calculated normal-force and pitching-moment characteristics of configuration C with inline and interdigitated canard surfaces are presented in figures 24 to 27. These comparisons show that method (1), employing slender-body theory for calculation of both the vortex paths and induced forces, generally gives the best estimate of the experimental normal force and pitching moment for these configurations either at an angle of attack or with the canard surfaces deflected. This result is to be expected from the fact that the wing is reasonably slender, having an effective aspect ratio of about 1 at a Mach number of 3.0, and that the calculated vortex paths are in good agreement

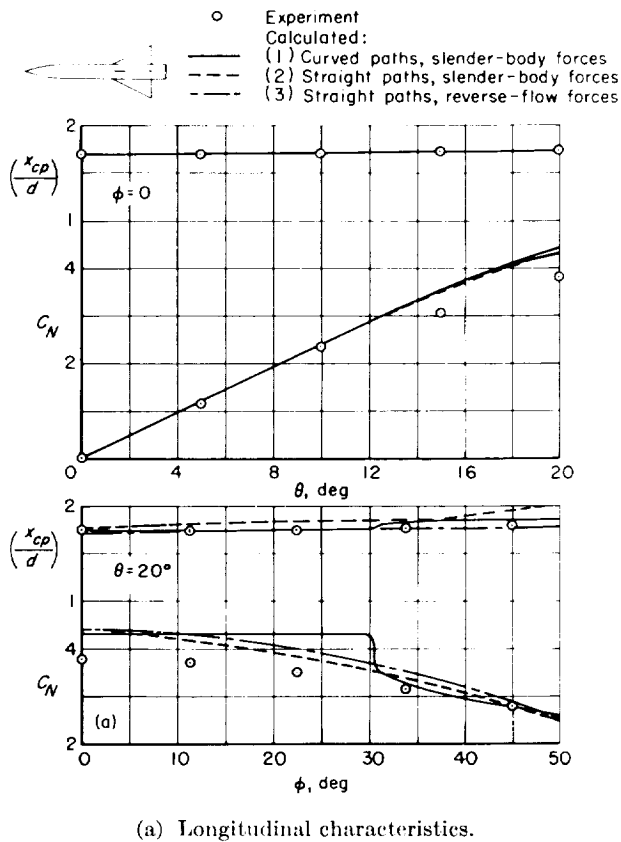


(b) Lateral characteristics.

FIGURE 22.—(Concluded).

with the measured paths, as previously discussed (fig. 12).

Comparisons between the experimental and calculated normal-force and center-of-pressure characteristics of configuration D are presented in figures 28 and 29 for two Mach numbers. Figure 28 shows that no significant differences exist among the three methods for predicting the normal force due to the canard vortices, but method (3) appears to give the best prediction of the center-of-pressure location, especially at a Mach number of 2.2. At this Mach number the effective aspect ratio of the wing is about 3.9 and hence the use of slender-body theory for calculating the vortex paths or forces would not be expected to be valid. The results shown in figure 29 indicate that in terms of the total forces and moments, no significant differences exist among the three calculative methods and that



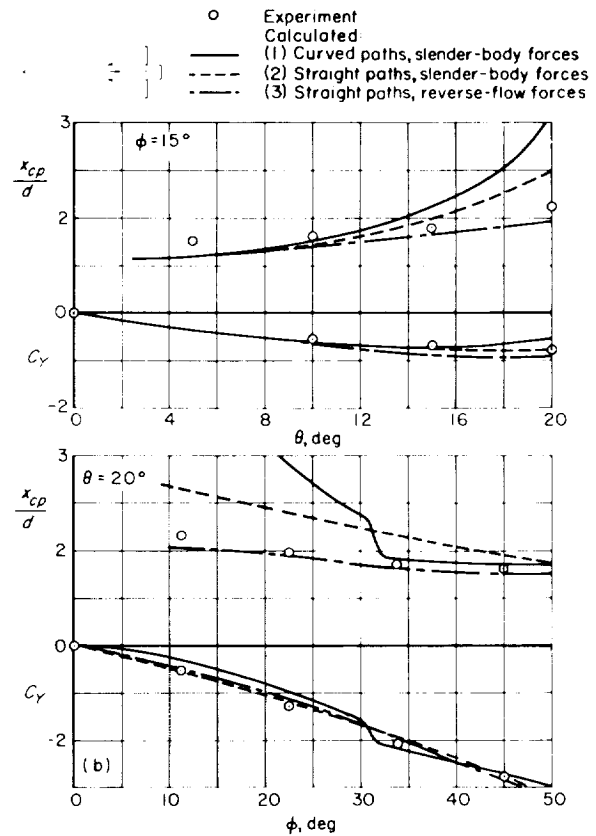
(a) Longitudinal characteristics.

FIGURE 23.—Comparison of calculated and experimental total forces and moments; configuration B; $M=2.0$.

the predicted values are in close agreement with the experimental results.

CONCLUDING REMARKS

A general method based on slender-body theory is developed for calculating the paths of vortices in the presence of wing-body combinations and the effects of these vortices on the aerodynamic loading, forces, and moments of the combinations at subsonic, transonic, and supersonic speeds. The method is applied to a family of triangular-wing and body combinations with systematic changes in the vortex strength, initial vortex position, angle of roll, angle of pitch, and wing aspect ratio. The method is evaluated by comparisons of the calculated vortex paths, forces, and moments with experimental results for several configurations and with the results calculated by alternate theoretical methods.



(b) Lateral characteristics.

FIGURE 23.—Concluded.

Results of the theoretical study showed that all the variables investigated had important effects on the calculated vortex paths. It was found that the closer a vortex approached the surface of a wing-body combination the more its position in the transverse plane changed as it moved downstream. The increased movement is due to the increasing predominance of the effect of the vortex image system over the effects of the potential crossflow and of the other vortices. For combinations having slender wings (leading edge well within the Mach cone) the experimental paths of vortices from canard surfaces were closely predicted, but for a combination having a nonslender wing (leading edge near the Mach cone) only qualitative predictions of the paths were obtained.

The calculated loading, forces, and moments due to vortices were influenced significantly by

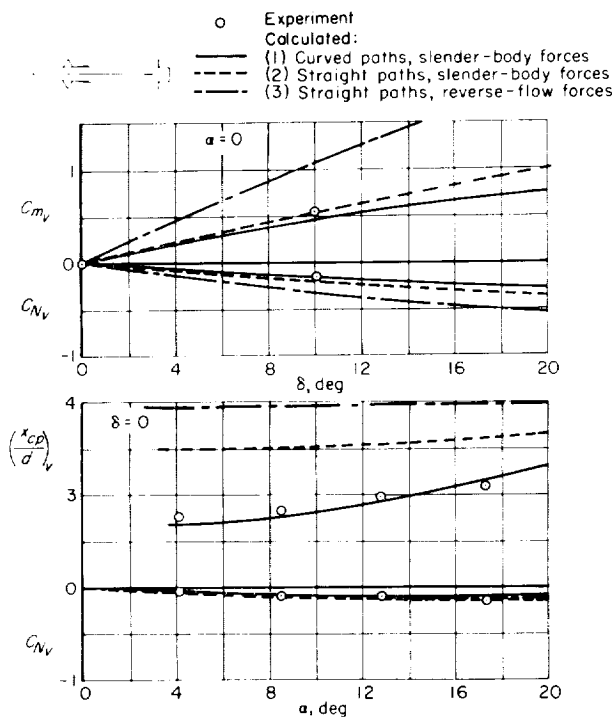


FIGURE 24.—Comparison of calculated and experimental forces and moments due to vortices; configuration C with inline canard surfaces; $M=3.0$.

changes in the variables investigated because of the resulting changes in the vortex paths and strengths. Calculated and experimental forces and moments induced by vortices from the fore-body or canard surfaces on three configurations were in good agreement for slender wing-body combinations. The agreement for two nonslender combinations, however, was only fair because of the failure of the vortices to follow closely the calculated paths and because of the use of slender-body theory for calculating the loads. The use of an alternate method based on vortex paths parallel to the body axis and on reverse-flow theory resulted in some improvements in the prediction of the vortex-induced forces and moments for nonslender combinations, but for slender configurations this method generally impaired the predictions. The total forces and moments acting on the various configurations were predicted closely in most cases by either theoretical method for calculating the vortex-induced forces and moments.

AMES RESEARCH CENTER

NATIONAL AERONAUTICS AND SPACE ADMINISTRATION
MOFFETT FIELD, CALIF., Jan. 16, 1961

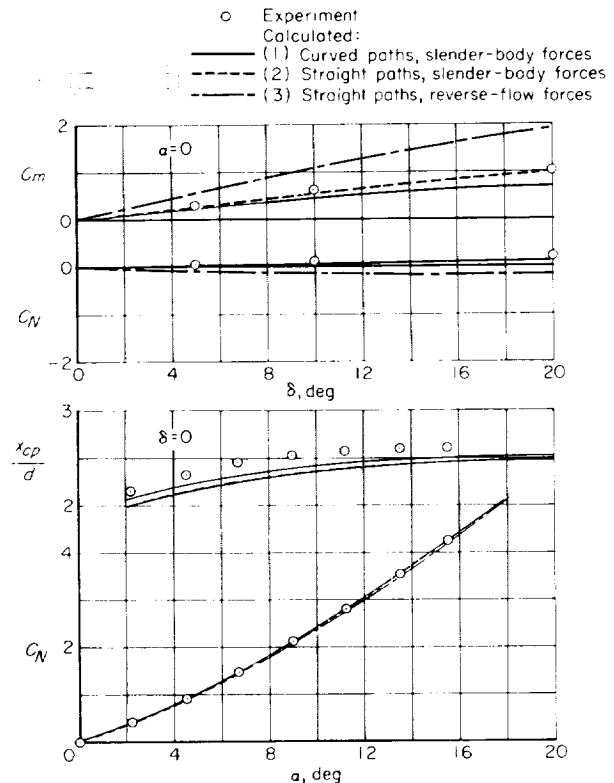


FIGURE 25.—Comparison of calculated and experimental total forces and moments; configuration C with inline canard surfaces; $M=3.0$.

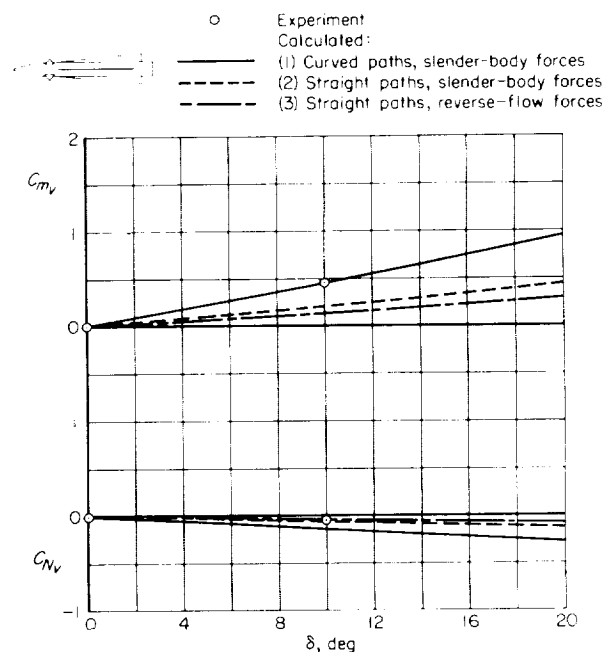


FIGURE 26.—Comparison of calculated and experimental normal force and pitching moment due to vortices; configuration C with interdigitated canard surfaces; $M=3.0$; $\alpha=0^\circ$.

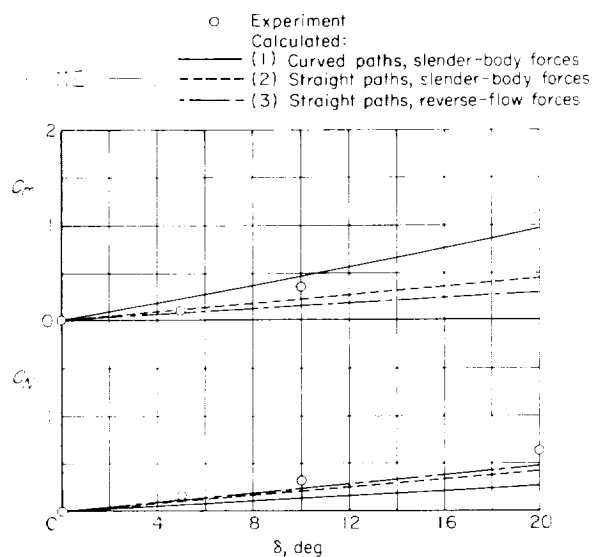
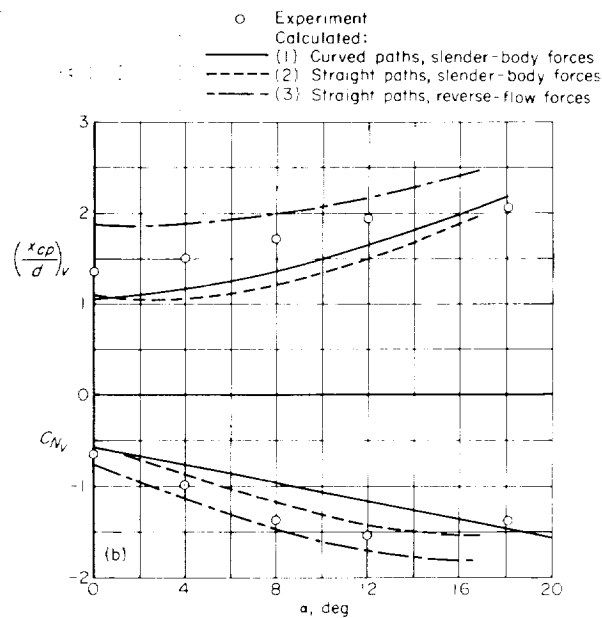
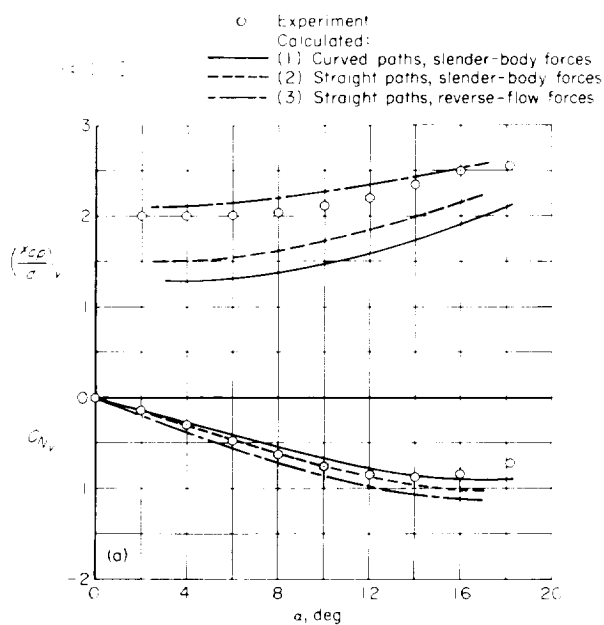


FIGURE 27.—Comparison of calculated and experimental total normal force and pitching moment; configuration C with interdigitated canard surfaces; $M=3.0$; $\alpha=0^\circ$.



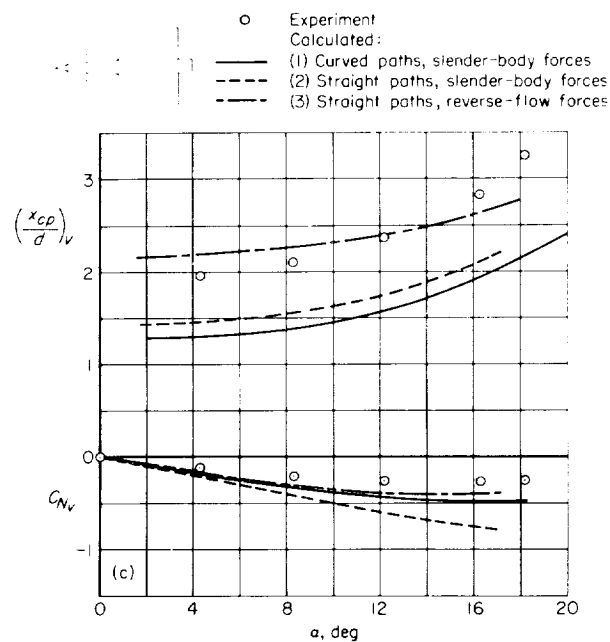
(b) $M=1.3$; $\delta=16^\circ$

FIGURE 28.—Continued.



(a) $M=1.3$; $\delta=0^\circ$

FIGURE 28.—Comparison of calculated and experimental normal force and center of pressure due to vortices; configuration D.



(c) $M=2.2$; $\delta=0^\circ$

FIGURE 28.—Continued.

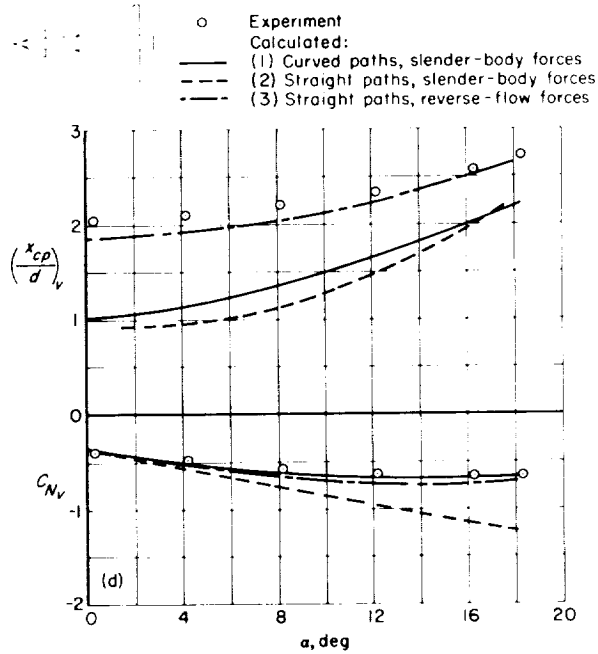
(d) $M=2.2$; $\delta=10^\circ$

FIGURE 28.—Concluded.

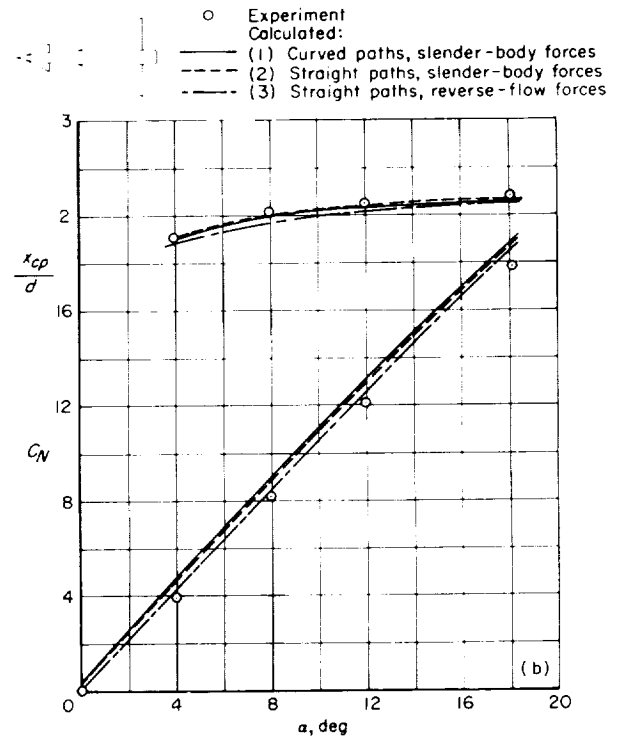
(b) $M=1.3$; $\delta=10^\circ$

FIGURE 29.—Continued.

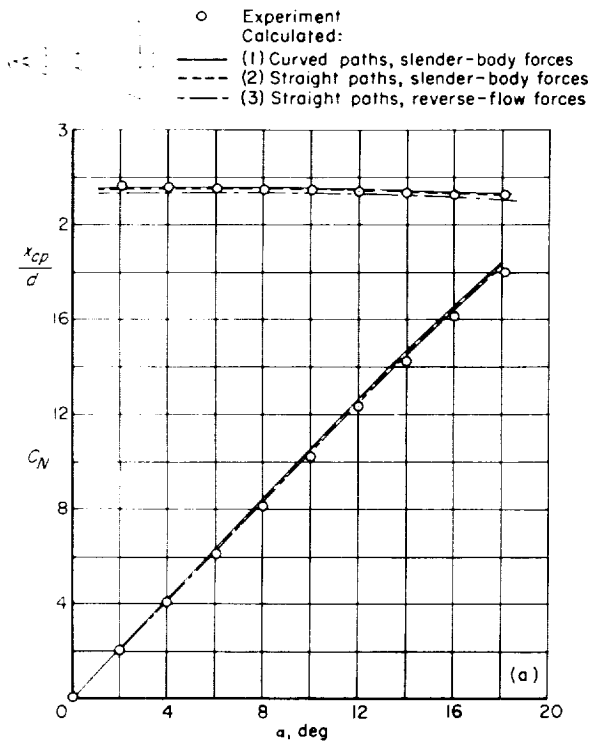
(a) $M=1.3$; $\delta=0^\circ$

FIGURE 29.—Comparison of calculated and experimental total normal force and center of pressure; configuration D.

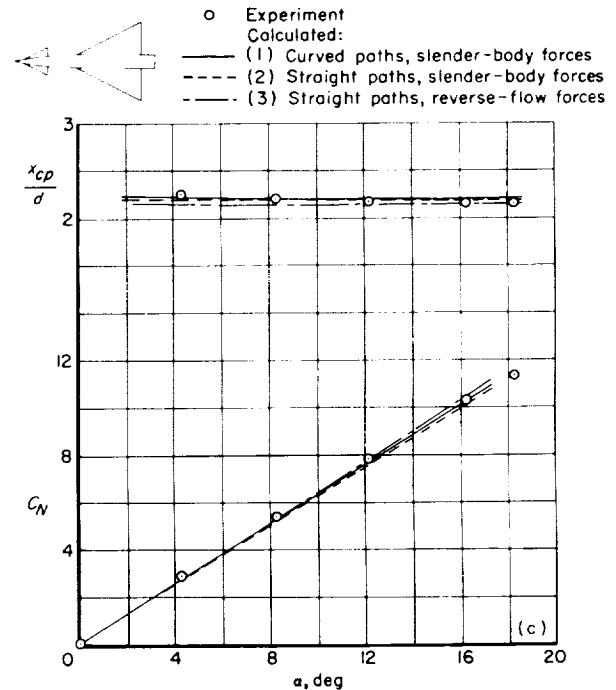
(c) $M=2.2$; $\delta=0^\circ$

FIGURE 29.—Continued.

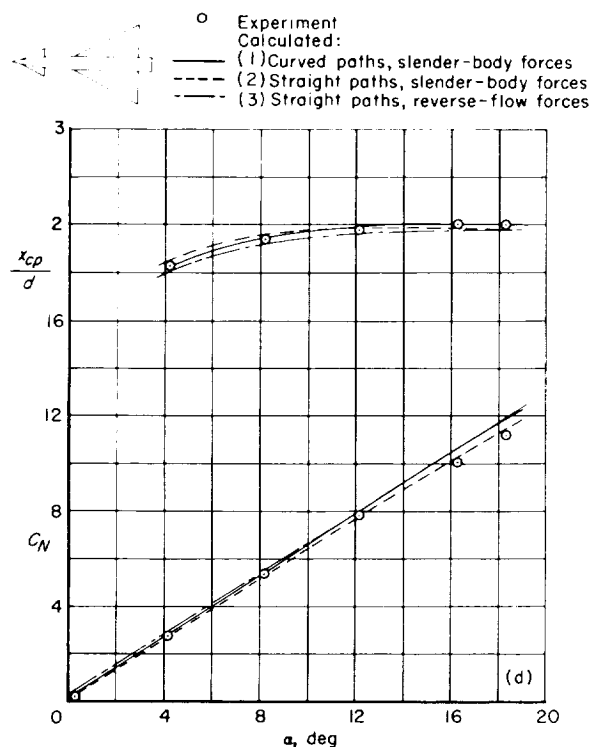


FIGURE 29.—Concluded.

REFERENCES

1. Spahr, J. Richard: Contribution of the Wing Panels to the Forces and Moments of Supersonic Wing-Body Combinations at Combined Angles. NACA TN 4146, 1958.
2. Pitts, William C., Nielsen, Jack N., and Kaattari, George E.: Lift and Center of Pressure of Wing-Body-Tail Combinations at Subsonic, Transonic, and Supersonic Speeds. NACA Rep. 1307, 1957.
3. Ursell, F., and Ward, G. N.: On Some General Theorems in the Linearized Theory of Compressible Flow. Quart. Jour. Mech. and Appl. Math., vol. III, pt. 3, Sept. 1950, pp. 326-348.
4. Heaslet, Max. A., and Spreiter, John R.: Reciprocity Relations in Aerodynamics. NACA Rep. 1119, 1953.
5. Sacks, Alvin H.: Vortex Interference on Slender Airplanes. NACA TN 3525, 1955.
6. Nielsen, Jack N., and Kaattari, George E.: The Effects of Vortex and Shock-Expansion Fields on Pitch and Yaw Instabilities of Supersonic Airplanes. IAS Preprint No. 743, 1957.
7. Jorgensen, Leland H., and Perkins, Edward W.: Investigation of Some Wake Vortex Characteristics of an Inclined Ogive-Cylinder Body at Mach Number 2. NACA Rep. 1371, 1958.
8. Rancy, D. J.: Measurements of the Cross Flow Around an Inclined Body at a Mach Number of 1.91. R.A.E. TN Aero. 2357, 1955.
9. Mello, J. F.: Investigation of Normal Force Distributions and Wake Vortex Characteristics of Bodies of Revolution at Supersonic Speeds. Jour. Aero/Space Sci., vol. 26, no. 3, March 1959, pp. 155-168.
10. Bryson, Arthur E., Jr.: Symmetric Vortex Separation on Circular Cylinders and Cones. Jour. Appl. Mech., vol. 26, no. 4, Dec. 1959.
11. Lin, C. C.: On the Motion of Vortices in Two Dimensions. Univ. of Toronto, Applied Math. Series, Study no. 5, 1943.
12. Miles, J. W.: On Interference Factors for Finned Bodies. Jour. Aero. Sci., vol. 19, no. 4, Apr. 1952, p. 287.
13. Kuerti, G., McFadden, J. A., and Shanks, D.: Virtual Mass of Cylinders with Radial Fins and of Polygonal Prisms. NAVORD Rep. 2295, 1952.
14. Bryson, Arthur E., Jr.: Evaluation of the Inertia Coefficients of the Cross Section of a Slender Body. Jour. Aero. Sci., vol. 21, no. 6, June 1954, p. 424.
15. Bryson, Arthur E., Jr.: The Aerodynamic Forces on a Slender Low (or High) Wing, Circular Body, Vertical Tail Configuration. Jour. Aero. Sci., vol. 21, no. 8, Aug. 1954, pp. 574-5.
16. Rogers, Arthur W.: Application of Two-Dimensional Vortex Theory to the Prediction of Flow Fields Behind Wings of Wing-Body Combinations at Subsonic and Supersonic Speeds. NACA TN 3227, 1954.
17. Boyd, John W., and Peterson, Victor L.: Static Stability and Control of Canard Configurations at Mach Numbers From 0.70 to 2.22—Longitudinal Characteristics of a Triangular Wing and Canard. NACA RM A57J15, 1958.
18. Spreiter, John R.: The Aerodynamic Forces on Slender Plane- and Cruciform-Wing and Body Combinations. NACA Rep. 962, 1950.
19. Spreiter, John R., and Sacks, Alvin H.: The Rolling Up of the Trailing Vortex Sheet and Its Effect on the Downwash Behind Wings. Jour. Aero. Sci., vol. 18, no. 1, Jan. 1951, pp. 21-32, 72.

TABLE I.—EXPRESSIONS FOR POTENTIAL-FLOW VELOCITY COMPONENTS ON SURFACES OF WING-BODY COMBINATIONS

Velocity component	Cruciform combination		Planar combination	
	Horizontal wing panels	Body	Wing panels	Body
$u_{wL} = -u_{wL}$	$V\alpha \left[\left(\frac{1-\frac{a^4}{s^4}}{(1+\frac{a^4}{s^4}) - \frac{y^2}{s^2}} - \frac{ds}{s^2} \left(1 + \frac{a^4}{y^4} \right) \right)^{1/2} \right]$	$V\alpha \left[\left(\frac{1-\frac{a^4}{s^4}}{(1+\frac{a^4}{s^2})^2 - 4\frac{y^2}{s^2}} - \frac{ds}{s^2} \right)^{1/2} \right]$	$V\alpha \left[\left(\frac{1-\frac{a^4}{s^4}}{(1+\frac{a^4}{s^4}) - \frac{y^2}{s^2}} - \frac{ds}{s^2} \left(1 + \frac{a^4}{y^4} \right) \right)^{1/2} \right]$	$V\alpha \left[\left(\frac{1-\frac{a^4}{s^4}}{(1+\frac{a^2}{s^2})^2 - 4\frac{y^2}{s^2}} - \frac{ds}{s^2} \right)^{1/2} \right]$
$v_{wL} = -v_{wL}$	$-V\alpha \left[\left(\frac{\frac{y}{s} \left(1 - \frac{a^4}{y^4} \right)}{(1+\frac{a^4}{s^4}) - \frac{y^2}{s^2}} - \frac{ds}{s^2} \left(1 + \frac{a^4}{y^4} \right) \right)^{1/2} \right]$	$V\alpha \left[\left(\frac{\frac{y}{s} \left(1 - \frac{y^2}{a^2} \right)}{(1+\frac{a^2}{s^2})^2 - 4\frac{y^2}{s^2}} - \frac{ds}{s^2} \right)^{1/2} \right]$	$-V\alpha \left[\left(\frac{\frac{y}{s} \left(1 - \frac{a^4}{y^4} \right)}{(1+\frac{a^4}{s^4}) - \frac{y^2}{s^2}} - \frac{ds}{s^2} \left(1 + \frac{a^4}{y^4} \right) \right)^{1/2} \right]$	$-V\alpha \left[\left(\frac{\frac{y}{s} \left(1 - \frac{y^2}{a^2} \right)}{(1+\frac{a^2}{s^2})^2 - 4\frac{y^2}{s^2}} - \frac{ds}{s^2} \right)^{1/2} \right]$
$w_{wL} + V\alpha = w_{wL} + V\alpha$	0	$V\alpha \left[\left(\frac{\frac{4}{s} \frac{y}{a} \left(1 - \frac{y^2}{a^2} \right)}{(1+\frac{a^2}{s^2})^2 - 4\frac{y^2}{s^2}} \right)^{1/2} \right]$	0	$V\alpha \left[\left(\frac{\frac{4}{s} \frac{y}{a} \left(1 - \frac{y^2}{a^2} \right)}{(1+\frac{a^2}{s^2})^2 - 4\frac{y^2}{s^2}} \right)^{1/2} \right]$
$v_{wL} - V\beta = v_{wL} - V\beta$	$-V\beta \left[\left(\frac{\frac{y}{s} \left(1 - \frac{a^4}{y^4} \right)}{(1+\frac{a^4}{s^4}) + \frac{y^2}{s^2}} - \frac{ds}{s^2} \left(1 + \frac{a^4}{y^4} \right) \right)^{1/2} \right]$	$-V\beta \left[\left(\frac{\frac{y}{s} \left(1 - \frac{y^2}{a^2} \right)}{(1+\frac{a^2}{s^2})^2 + 4\frac{y^2}{s^2}} - \frac{ds}{s^2} \right)^{1/2} \right]$	$-V\beta \left(1 - \frac{a^2}{y^2} \right)$	$-2V\beta \left(1 - \frac{y^2}{a^2} \right)$
$w_{wL} = -w_{wL}$	0	$V\beta \left[\left(\frac{\frac{y}{s} \left(1 - \frac{y^2}{a^2} \right)}{(1+\frac{a^2}{s^2})^2 + 4\frac{y^2}{s^2}} - \frac{ds}{s^2} \right)^{1/2} \right]$	0	$2V\beta \frac{y}{a} \left(1 - \frac{y^2}{a^2} \right)^{1/2}$

TABLE II.—VORTEX STRENGTHS AND INITIAL POSITIONS ($x=0$)

Configuration	M	θ , deg	φ , deg	C_T	$\left(\frac{y_r}{a}\right)_1$	$\left(\frac{z_r}{a}\right)_1$	$\left(\frac{y_r}{a}\right)_2$	$\left(\frac{z_r}{a}\right)_2$
B	2.0	15	0	0.147	0.62	1.15	-0.62	1.15
		20	0	.263	.68	1.46	-.68	1.46
		20	7.5	.263	.48	1.54	-.87	1.36
		20	15.0	.263	.28	1.59	-1.04	1.23
		20	22.5	.263	.07	1.61	-1.19	1.09
		20	30.0	.263	-.14	1.60	-1.32	.92
		20	37.5	.263	-.35	1.57	-1.43	.74
		20	45.0	.263	-.55	1.51	-1.51	.55
		15	15.0	.147	.30	1.27	.90	.95
Configuration	M	α , deg	δ , deg	C_T	$\left(\frac{y_r}{a}\right)_1$	$\left(\frac{z_r}{a}\right)_1$	$\left(\frac{y_r}{a}\right)_2$	$\left(\frac{z_r}{a}\right)_2$
C In-line	3.0	0	10	.026	1.63	-.06	-1.63	-.06
		0	20	.054	1.60	-.12	-1.60	-.12
		10	0	.039	1.63	0	-1.63	0
		15	0	.060	1.61	0	-1.61	0
		20	0	.082	1.60	0	-1.60	0
C Interdigitated	3.0	0	10	.020	1.12	1.12	-1.12	1.12
		0	20	.040	1.12	1.12	-1.12	1.12
D	1.3	∞	0	.072	1.63	.48	-1.63	.48
		16	0	.162	1.51	.93	-1.51	.93
		0	10	.062	1.60	.39	-1.60	.39
		∞	10	.154	1.49	.05	-1.49	.05
		16	10	.270	1.37	.44	-1.37	.44
	2.2	∞	0	.048	1.63	.51	-1.63	.51
		16	0	.101	1.51	1.02	-1.51	1.02
		0	10	.046	1.60	.37	-1.60	.37
		∞	10	.108	1.49	.11	-1.49	.11
		16	10	.118	1.37	.58	-1.37	.58

